Comparison of debris-flow observations, including fine sediment grain size and composition, and runout model results at the Illgraben, Swiss Alps

[1,2]Daniel Bolliger, [1]Fritz Schlunegger*, [3]Brian W. McArdell

[1]Institute of Geological Sciences, University of Bern, Switzerland

[2]Geotest AG, Zollikofen, Switzerland

[3]Swiss Federal Institute WSL, Switzerland

*Corresponding author: fritz.schlunegger@unibe.ch

Abstract

Debris flows are important processes for the assessment of natural hazards due to their damage potential. To assess the impact of a potential debris flow, parameters such as the flow velocity, flow depth, maximum discharge and the volume are of great importance. This study uses data from the Illgraben observation station, Central Alps of Switzerland, to explore the relationships between these flow parameters and the debris flow dynamics. To this end, we simulated previous debris flow events with the RAMMS debris flow runout model, which is based on a numerical solution of the shallow water equations for granular flows using the Voellmy friction relation. Here, the events were modeled in an effort to explore possible controls on the friction parameters μ and ξ, which describe the Coulomb friction and the turbulent friction, respectively, in the model. Additionally, sediment samples from levee deposits were analyzed for their grain size distributions (14 events) and their mineralogical properties (four events) to explore if the properties of the fine-grained matrix have an influence on the debris flow dynamics. Finally, field data from various debris flows such as the flow velocities and depths were statistically compared with the grain size distributions, the mineralogical properties, and the simulation results to identify the key variables controlling the kinematics of these flows. The simulation results point to several ideal solutions, which depend on the Coulomb and turbulent friction parameters (μ and ξ, respectively). In addition, the modelling results show that the Coulomb and turbulent frictions of a flow are related to the Froude number if the flow velocity is < 6-7 m/s. It is also shown that the fine-sediment grain size or clay-particle mineralogy of a flow neither correlates with the flow's velocity and depth, nor can it be used to quantify the friction in the Voellmy friction relation. This suggests that the frictional behavior of a flow may be controlled by other properties such as the friction generated by the partially fluidized coarse granular sediment. Yet, the flow properties are well-correlated

Deleted: Modelling
Deleted:
Deleted: runout considering
Deleted: distributions of debris flows
Formatted: Font: Bold, English (US)
Formatted: Font: Bold, English (US)
Formatted: Font: Bold, English (US)
Formatted: Normal, Left, Line spacing: single
Formatted: Font: Bold, English (US)
Formatted: Left, Line spacing: Multiple 1.25 li
Formatted: German (Switzerland)
Deleted: The flows were
Deleted: basal
Deleted: viscous
Deleted: (ii)
Deleted: the existence of
Deleted: with the
Deleted: showing
Deleted: strong dependency on
Deleted: of
Deleted: no statistically significant correlation exists between the
Deleted: distribution, the mineralogical composition of the matrix, and the debris flow properties, confirming the notion that a fixed debris-
Deleted: or rheology is
Deleted: limiting assumption, at least for the Voellmy relation. Rather
Deleted: appear to be determined by

with the flow volume, from which most other parameters can be derived, consistent with common engineering practice.

1 Introduction

1.1 Debris flows, and parameters controlling their velocity and runout

Debris flows are rapid mass movements consisting of water-saturated and poorly sorted debris with a large range of grain sizes. Debris flows tend to develop one single or a suite of multiple surges with steep coarse-grained fronts. Their motion is driven by gravity and resisted by friction within the flow and at the boundary with the channel bed (Iverson, 1997). The boulder-rich front is then followed by a tapering body where the pore fluid pressures are large, often exceeding the hydrostatic pressure (Iverson, 1997, McArdell et al., 2007). In the frontal part, larger particles tend to ascend in the debris flow body due to particle collisional stresses thereby building a coarse-grained top layer (Johnson et al., 2012), which travels somewhat faster than the flow front itself, delivering coarse sediment to the front. Accordingly, the coarser-grained particles along with some of the fine sediment present at the surface of the flow tend to accumulate in the surge head and are deposited laterally in levees just a few meters behind the front (Johnson et al., 2012).

In the past years, de Haas et al. (2015) conducted experiments to investigate how the grain size distribution and water content influences the velocity of a debris flow. They found that a higher clay content tends to result in an increase of both the velocity and the runout distance of such flows. However, if the clay content becomes too large, then the velocity decreases due to a higher viscosity of the fluid. This relationship should also be applicable to the silt fraction because clay and silt particles are a part of the fluid while grains larger than silt contribute to the solids of a debris flow (Iverson, 1997). The experiments of de Haas et al. (2015) also showed that a large gravel content in the flow front leads to a strong frictional resistance, which in turn reduces the flow velocity. In addition, a large gravel content results in a larger pore water diffusivity, which reduces the pore pressure in the flow and contributes to a further reduction of the flow velocity. On the other hand, a low gravel content leads to lower collisional forces, which might also lead to a relatively low flow velocity. Furthermore, also according to the experiments by de Haas et al. (2015), the water content, the velocity, the volume, and the runout distance of a debris flow are positively correlated to each other. Based on a combination of experimental and field data, Hürlimann et al. (2015) came to the same conclusions, and they additionally found that an increase in the clay content generally leads to a reduction in the runout distance. Indeed, the absorption of water in swelling clay minerals has the potential to result in an increase of the cohesion of a flow, which in turn could cause a reduction of the flow velocity and the runout distance. Finally, using laboratory experiments, Kaitna et al. (2016) documented that a relatively high fraction of fine-grained material tends to occur in flows with excess pore fluid pressures. In addition, these authors mentioned that such flows were characterized by low fluctuations of normalized fluid pressures and normal stresses, and the experiments showed that the shear stresses were concentrated

Deleted: <#>*Debris flow processes*¶

Deleted: Flows

Deleted: larger

Deleted: with low pore fluid pressures, and their

Deleted: high

Deleted: There

Deleted:). Such aggregation of larger boulders is mainly due to strong buoyancy forces caused by the laminar

Deleted: in the

Deleted: , which results in a grain-size segregation and thus in a shift of the larger particles

Deleted: and the top of the flow. In addition, because this top layer tends to have a larger flow velocity than the debris flow front, the fine-grained material in the surge head is preferentially reincorporated into the body, whereas

Deleted:).

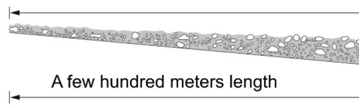

Deleted:
Figure 1: General architecture of a debris flow modified after Pierson (1986).¶
¶
Parameters controlling debris flow processes¶

Deleted: De

Deleted: dynamics

Deleted: thus the mobility

Deleted: Following de Haas et al. (2015), we thus expect a distinct ratio between the clay and gravel contents that allows a flow to reach a maximum velocity.

Deleted: In addition, these authors demonstrated that a larger volume leads to an increase in the flow velocity. The study of Hürlimann et al. (2015), based

Deleted: suggests a positive correlation between volume, water content

Deleted: runout distance. They

at the base of the flow. Based on the conclusions of the aforementioned authors, we expect to see a dependency of the flow properties in the Illgraben and the granulometric composition of these flows (Uchida et al., 2012), and we anticipate that the flow velocity is negatively correlated with the relative abundance of the finest-grained particles.

The mineralogical composition of a flow is a further parameter, which has the potential to impact the rheology and thus the flow velocity and runout distance of debris flows, yet these relationships have largely been overlooked in the literature. In particular, because clay minerals are important constituents of the fine-grained fraction of these flows, they have the potential to regulate the pore fluid pressure and the stress state through their ability to absorb water in their crystal structure (Di Maio et al., 2004). This is mainly the case for swelling clay minerals (see also section above) such as those of the smectite group (Di Maio et al., 2004), where the pore fluid composition has a large influence on the volume and the shear strength of these minerals (Chatterji and Morgestern, 1990; Di Maio, 1996). Because shear stresses within a flow are a direct consequence of the friction between the particles and the fluid phase and since the friction properties directly influence the propagation of a debris flow (see section 1.2), we anticipate the occurrence of a direct relationship between the velocity and runout distance of debris flows, and the mineralogical composition of the fine-grained matrix.

1.2 Physically-based models describing debris flow processes, and goal of paper

There are several rheological models or flow resistance relationships describing the behavior of debris flows such as the flows' velocities, runout distances and frictional properties (e.g., Allen, 1997; Rickenmann, 1999; Naef et al., 2006). One commonly used approach is the Voellmy friction relation (Voellmy, 1955; Salm, 1990; 1993; Christen et al., 2012), which is also implemented in the software RAMMS, a software package to simulate debris flow runout (see section 3.1). In the Voellmy friction equation, the frictional resistance of a flow S [Pa] is composed of the sum of two friction terms: (i) A dry Coulomb-type friction term, referred to as Coulomb friction, describes the frictional resistance between the debris flow and the channel bed and mainly depends on the flow depth; and (ii) a drag or viscous-turbulent friction term describes the turbulent frictional resistance, which mainly depends on the dynamic pressure and thus on the velocity of the flow. Both components are characterized by the coefficients μ and ξ, which control the values of the Coulomb and the turbulent frictions, respectively (Christen et al., 2012). Optionally, cohesion stresses can be included in an extended Voellmy friction equation (Bartelt et al., 2015; Berger et al., 2016). Because this additional cohesion term has rarely been used in engineering practice and is apparently relatively small (Berger et al., 2016), it was neglected herein, and the friction equation takes the following form:

$$S = \mu N + \frac{\rho g v^2}{\xi}, N = \rho g h \cdot \cos(\varphi) \quad (1).$$

Formatted: Font colour: Auto

Deleted: ¶ Physical-mathematical

Deleted: Due to the complexities outlined above, the quantitative process description of debris flows has been a challenge.

Deleted: such flows

Deleted: *(1)*

Deleted: processes

Deleted: next

Deleted: internal

Deleted: value

Deleted: -type

Deleted: viscous-

Deleted: friction terms

Deleted: ¶ $S = \mu N + \frac{\rho g v^2}{\xi}$ $with\ N = \rho h g \cos(\varphi)$ ... [1]

where S is the frictional resistance [Pa], ρ the density of the debris flow, h the flow height (or flow depth), g the gravitational acceleration, φ the slope angle of the channel bed, and v the velocity of the flow.

A simplified approach to characterize a debris flow is the Froude number, which describes the ratio between the inertial and the gravitational forces:

$$Fr = \frac{v}{\sqrt{gh}} \quad (2),$$

where Fr is the Froude number, v the velocity of the flow, g the gravitational acceleration and h the flow height (Hübl et al., 2009; Choi et al., 2015).

As mentioned above, the velocity and runout distance of debris flows are likely to depend on the frictional resistance in such mass movements. This friction, in turn, can be characterized by two coefficients μ and ξ in the Voellmy friction relation (*1*). Because we anticipate that the mineralogical and granulometric composition of the fine-grained matrix has an influence on the properties of such flows (see section 1.1), we expect to identify a relationship between the frictional properties of a flow, its velocity, and its grain size and mineralogical composition. Here, we test and explore these hypotheses using in-situ data collected at the Illgraben debris flow monitoring station situated in the Central European Alps (Figure 1), and we evaluate the data with the results of a numerical runout model referred to as RAMMS. Upon combining field data with modelling results, we aim at identifying those parameters that have the largest control on the dynamic properties of the debris flows at the Illgraben.

2 Study site and setting

The Illgraben catchment is located in the Valais region in western Switzerland (Figure 1). It extends from the summit of the Illhorn (2716 m asl) to the outlet of the Illgraben into the Rhone River (610 m asl). The total area of about 9.5 km^2 consists of the Illgraben basin, which has a spatial extent of 4.6 km^2, and the Illbach tributary catchment covering 4.9 km^2 (Figure 1a). The Illgraben basin has been very active and has generated several debris flows each year (Schlunegger et al., 2009; McArdell and Satori, 2022). The rates of sediment discharge in the Illgraben have been exceptionally high for Alpine standards (Berger et al., 2011a). Several studies showed that the erosion rates and the numbers and extents of debris flows strongly depend on the hydro-climatic parameters such as the average annual temperature and the precipitation rates (Bennett et al., 2013; Hirschberg et al., 2019; 2021a, b).The highly fractured bedrock (Bumann, 2022), belonging to the Penninic nappe stack (Gabus et al., 2008), consists of massive-bedded limestones, quartzites and Triassic schists with dolobreccia interbeds. Schlunegger et al. (2009) considered these lithologies to be the main source of the silt and clay fraction that constitute the matrix of the debris flow deposits. Based on a petrographic analysis of the debris flow deposits, these authors also identified two distinct sediment sources

Deleted: ¶

Deleted: dimensionless

Deleted: *(2)*,

Deleted: forces

Deleted: ¶
$Fr = \frac{v}{\sqrt{gh}}$ ... [2]

Moved down [1]: (Christen et al., 2012; Bartelt et al.

Moved down [2]: 2015; Christen et al.,

Deleted: ¶
Modellling debris flow with RAMMS¶
As mentioned above, a widely applied tool to simulate debris-flow runout is the RAMMS software, which was developed by the Swiss Federal Institute for Forest, Snow and Landscape Research, WSL (WSL, 2022). RAMMS is based on the two-parameter Voellmy-fluid model

Deleted: 2015). This approach has been successfully applied to snow avalanches, landslides, and debris flows. A major challenge for modelling is the choice of input friction coefficients. If the simulation cannot be calibrated with data that were collected from a previous well-documented event (Christen et al., 2012; Deubelbeiss & Graf, 2011), the input parameters have to be estimated. Because the model results such as the velocity, the run-out distance, and the flow depth are very sensitive to the friction parameters μ and ξ (Bartelt et al., …

Deleted: 2012), the focus of this work is testing RAMMS with high-accuracy field data, including the grain size of specific flows. This is accomplished for the Illgraben debris flow observation station situated in the Central European Alps (McArdell and Sartori, 2021), because data on the thickness, velocity, and density of the flows have been continuously collected in the past years by the WSL (e.g., de Haas et al., 2022). An additional goal is to explore whether the grain size distribution and the mineralogical composition of the debris flow material have an influence on the flow dynamics, because these parameters have been considered as crucial for the understanding of the flow dynamics (see section 1.2).¶

Deleted: , which is the focus of this study,

Deleted: (Figure 2).

Deleted: Illbach basin covering 4.9 km^2 and the

Deleted: (Figure 2a). This latter sub-

Deleted: , which were

Deleted: (Schlunegger et al., 2009).

in the Illgraben, where bedrock lithologies with different petrological properties are exposed. These are (i) a heavily fractured and foliated suite of gneisses and schists, which are exposed on the southern flank of the Illgraben, and (ii) a vertically plunging succession of limestones, dolomites and cellular dolomites, which make up the northwestern flank of the Illgraben (Figure 1). The material from these two sources is very well mixed in response to repeated deposition and remobilization of sediment within the catchment (Schlunegger et al., 2009). The sediment cascade has been subject to seasonal variations, where smaller debris flows events are associated with net sediment accumulation in the channel, while large flows can entrain sediment up to several times their initial mass along their flow paths (Berger et al., 2010; Berger et al., 2011a, b; Schürch et al., 2011).

Grain size analyses conducted on samples from the channel bed and debris flow deposits indicated sand contents of 35-40% and clay contents of < 5% (Hürlimann et al., 2003; Schlunegger et al., 2009; Uchida et al., 2021). In the Rhone valley, an alluvial fan has formed covering an area of 6.6 km^2 (Schürch et al., 2016). The channel on the fan has a U-shaped cross-sectional geometry with a base that is about 5–10 m wide. For the lowermost 2 km, the gradient of the Illgraben channel ranges from about 7% to 18% (measured over a length of 50 m) with a mean of about 8% (Schlunegger et al., 2009). Thirty-one check dams with vertical drops of up to several meters were constructed along the lowermost 4.8 km of the channel to prevent the flows to further incise into the substratum (McArdell et al., 2007; Badoux et al., 2009). A debris flow monitoring station, situated on the lower fan c. 200 m upstream of the confluence with the Rhone River, was installed in 2000 and has been operated by the WSL since then (Hürlimann et al., 2003; Badoux et al., 2009). At the survey site (Figure 1c), the measured parameters include frontal velocity, flow depth, bulk density, maximum discharge rate, volumes, and normal and shear force (McArdell et al., 2007; McArdell 2016). The related values are presented in the openly accessible database of the WSL (McArdell et al., 2023), and the data was collected using the methods presented in section 3.1. On average 3 to 5 debris flows have been registered by the measuring station every year. They have generally occurred during intense rainstorms between May and October (e.g., McArdell et al., 2007).

Deleted: .

Deleted: is

Deleted: collected

Deleted: 31

Deleted: (Figure 2c),

Deleted:)

Deleted: .

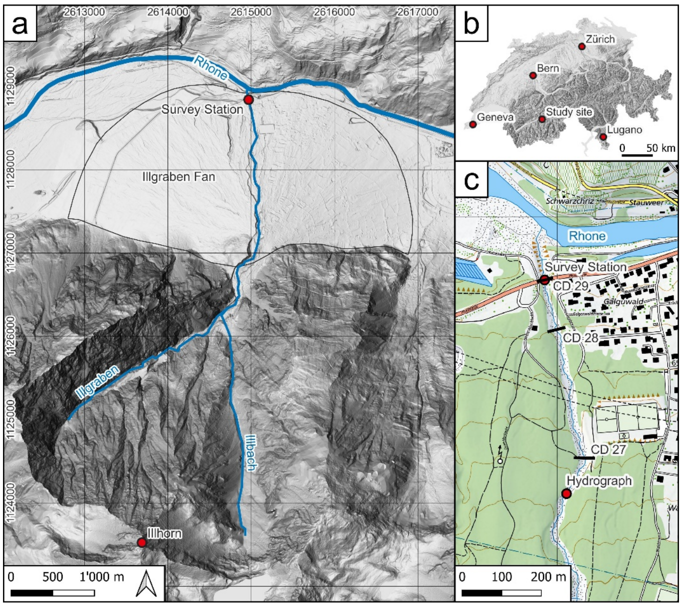

Figure 1: (a) Overview of the topographic situation around the Illgraben showing the Illgraben system with its river network consisting of the Illgraben, Illbach and the Rhone River. (b) Overview map of Switzerland with location of the study site. (c) Detailed topographic map of the Illgraben reach along which the RAMMS simulations have been conducted. It shows the location of the input hydrograph which was used as starting position for the modelling. The three check dams (CD) and the location of the survey station below the Pfynstrasse are displayed on this figure. The background is provided by the swissALTI3D and the Swiss Map Raster 10 (Swisstopo, 2022).

3 Methods

Using data collected in the field (section 3.1), we explored how the frictional properties of a debris flow influences the behavior (flow depth and velocity) of such a flow through modelling with RAMMS (section 3.2). We then tested whether the grain size distribution (section 3.3) and the mineralogical composition of the debris flow material (section 3.4) have an influence on the flow velocity.

3.1 Surveys of debris flows

Many of the in-situ measurements of the debris flow properties at the Illgraben have been accomplished with a force plate that is installed in the channel beneath a bridge c. 200 m upstream of the confluence with the Rhone River (survey station, see Figure 1c). At that survey site, information on (i) the velocity, (ii) the flow depth, (ii) the mean bulk density, (iii) the duration of individual debris flows, and (iv) the volumes of each flow have been determined in the past years by the WSL (e.g., McArdell and Sartori, 2021; de Haas et al., 2022, Belli et al., 2022; McArdell et al., 2023). As outlined in McArdell et al. (2007) and Schlunegger et al. (2009), the force plate is a horizontal 8 m^2 steel structure, which is installed flush with the river

Deleted: 2:

Deleted: In addition, the

Deleted: Because the flow

Formatted: Font colour: Black

bed just on the top of the concrete check dam. The plate is equipped with normal and shear force transducers. The flow depth is estimated using either a laser or radar unit. Because the radar data is biased by an unpredictable smoothing of the flow surface, we preferentially used the laser data for further calculations. Based on information about the flow depth and the normal force, it was possible to determine the bulk density of a flow as it moves on the plate itself. The volume of each flow was then calculated as the product between the velocity and the cross-sectional area, and this product was integrated over the flow's duration (McArdell et al., 2023). The frontal velocity is determined using the travel time of the flow front over the reach upstream of the force plate (between check dams 27 or 28 and 29; Figure 1c and Hürlimann et al., 2003). Appendix A presents a list of parameters, which been measured at the Illgraben monitoring site, and Appendix B for screenshots from video recordings of selected debris flows.

3.2 Numerical modelling with RAMMS

We explored, through modelling with RAMMS, how the frictional properties of a debris flow influence its behavior such as flow depth and velocity. The RAMMS model was developed by the Swiss Federal Institute for Forest, Snow and Landscape Research, WSL (WSL, 2022). It is based on the two-parameter Voellmy-fluid model (Christen et al., 2012; Bartelt et al. 2015), which describes the friction in the 2D depth-averaged equations of motion, which were deviated for granular flows. We justify the selection of such an approach because in an independent modelling study (FLATModel) calibrated with field data (Medina et al., 2007), the Voellmy-fluid formula (eq. *1*) has been proven to reproduce the dynamics of debris flows (flow velocity, erosion pattern in the channel, and aerial extension of the flow in the accumulation zone) reasonably well. A major challenge for modelling is the choice of the input friction coefficients. In particular, if the simulation cannot be calibrated with data that were collected from a previous well-documented event (Christen et al., 2012; Deubelbeiss & Graf, 2011), the input parameters have to be estimated. Because the model results such as the velocity, the runout distance, and the flow depth are sensitive to the friction parameters μ and ξ (Bartelt et al., 2015; Christen et al., 2012), we iteratively changed the values of these coefficients until we found, for each event, a best fit between the simulation results and the observations (Appendix C).

The Coulomb friction coefficient μ is sometimes expressed as the tangent of the internal shear angle (WSL, 2022). According to Salm (1993) an internal movement parallel to the slope is only possible if the internal shear angle is smaller than the slope angle. Consequently, the value of μ should be smaller than the tangent of the channel slope angle. For a minimum slope angle of 7% (4°), μ should thus be smaller than 0.07. Therefore, for every debris flow event, we conducted

Moved (insertion) [3]

Moved (insertion) [1]

Deleted: depend on the values of

Moved (insertion) [2]

Deleted: , we conducted simulations with the RAMMS software and …

Deleted: μ and ξ

Formatted: Font: Not Italic

Deleted: . These simulations will allowed us to identify those pairs of friction parameters that best explain the measured conditions of the simulated flows (such as the flow velocity and the flow depth). We then tested the dependency of the input parameters on the measured debris flow properties using statistical methods and the software Matlab (R2021b). Because we hypothesize that the grain size distribution of the fine-grained fraction, and possibly the mineralogical composition of the debris flows, influence the friction of the flow, we finally tested these relationships using grain size and XRD data collected from the flow deposits.

Moved up [3]: ¶
Numerical modelling with RAMMS¶

Moved down [4]: In addition, a filter (Serval-Raster editing tools, version 3.10.2) was applied to the channel bed to smoothen the bed surface.

Moved down [5]: Erosion was allowed to occur along the entire channel (Frank et al.,

Deleted: The use of RAMMS requires a digital elevation model (DEM), event volume and peak discharge. The drone-based DEM, which is based on a survey conducted on the 10th of August 2021 (de Haas et al., 2022), was used for all simulations. However, this high-resolution DEM did not cover the section of the channel between the Pfynstrasse and the Rhone River (Figure 2c). Therefore, in order to extend the area towards the confluence with the Rhone, the photogrammetry DEM was combined with an existing 0.5 m-lidar DEM (Swisstopo, 2022) using the software QGIS. The DEM of the short, concrete channel section beneath the road bridge had to be reconstructed manually since it was not possible to image the topography below the bridge.

Deleted: This was done because a large local change in topography (such as a boulder) can induce strong vertical accelerations in RAMMS, which can lead to unrealistically large (or small) local flow depths. ¶
We employed the 'hydrograph' input option of RAMMS to model the flows, which releases a completely developed debris flow with user-specified velocity, volume, density, and time-dependent discharge values. The hydrograph input was placed upstream of the football field c. 500 m upstream of the survey site (check dam 27, Figure 2c).

Deleted: %, which is equivalent to

Deleted: °,

several simulations (between 12 and 43, Appendix C) with μ varying from 0.01 to 0.06, and we modified the ξ parameter to minimize the *z*-value, which is explained with eq. (3) below. This resulted in μ–ξ pairs with lowest z-values and thus best fits between the model results and observations (such as the flow velocity *v* and the flow depth *h*). Please see Appendix C for information about the number of modelling runs, the intervals between the μ– and ξ–values, and other input parameters that we used upon modelling.

We employed the 'hydrograph' input option of RAMMS to characterize the debris flows in the model. Upon modelling, the hydrograph input was placed c. 500 m upstream of the survey site (check dam 27, Figure 1c). Erosion was allowed to occur along the entire channel (Frank et al., 2015; 2017) except at the check dams. Similar to the surveys in the field (section 3.1), the model velocity was calculated using the travel time between check dams 28 and 29 (Figure 1c). The modelled flow depth values used herein were obtained as the average of the measurements that were conducted at four points along a cross section at check dam 29.

The use of RAMMS requires a digital elevation model (DEM), event volume, and peak discharge. The drone-based DEM, which is based on a survey conducted on the 10th of August 2021 (de Haas et al., 2022), was used for all simulations. However, this high-resolution DEM did not cover the section of the channel between the Survey Station and the Rhone River (Figure 1c). Therefore, in order to extend the area towards the confluence with the Rhone River, the photogrammetry DEM, which has resolution of 0.1 m, was combined with an existing 0.5 m-lidar DEM (Swisstopo, 2022) using the software QGIS. Here, we resampled the drone-based DEM to achieve the same resolution as the lidar DEM of Swisstopo (i.e., 0.5 m) so that both datasets could be combined. The DEM of the short, concrete channel section beneath the road bridge had to be reconstructed manually because it was not possible to image the topography below the bridge. In addition, a filter (Serval-Raster editing tools, version 3.10.2) was applied to the channel bed to smoothen the bed surface. This was done because a large local change in the topography (such as a boulder) can induce strong vertical accelerations in RAMMS (and other models that are based on the depth-averaged equations of motion), which can lead to unrealistically large (or small) local flow depths.

Finally, we introduced a dimensionless *z*-value to describe the deviation of the simulated velocity *v* and flow depth *h* from the measurements in the field:

$$z = \sqrt{\left(\frac{v_{simulation} - v_{measured}}{v_{measured}}\right)^2 + \left(\frac{h_{simulation} - h_{measured}}{h_{measured}}\right)^2} \qquad (3).$$

We thus explored how the model input parameters (μ– and ξ–values) affect the modelled velocity and depth values of a flow. We then compared the model results with the surveyed velocities and depths of each flow using eq. (3), which we implemented in the software Matlab (R2021b).

Deleted: .

Moved (insertion) [5]

Moved (insertion) [4]

3.3 Grain size distribution

For most of the debris flows that occurred in the years 2019, 2021 and 2022, at least one sediment sample of 1.5 to 3 kg was taken from the levee deposits at the same site labelled as 'Survey Station' in Figure 1c (Swiss coordinates: 2'614'973, 1'128'842; Figure 1c). We collected the material from underneath the bridge to prevent effects related to grain-size-dependent erosion by rainfall. We selected the levee deposits for three reasons. First, according to our experience, the levee deposits can better be attributed to a specific event than other sediments of a debris flow. Second, the levee deposits are those sediments of a debris flow that most clearly record the granulometric composition of the surge head, as our observations on video recordings have shown. Third, it is the surge head, which exerts the greatest control on the dynamics of a debris flow (McArdell et al., 2007; Johnson et al., 2012). Accordingly, upon collecting material from levee deposits, we are likely to analyze sediments with the highest potential to provide information that allows us to understand the dynamics (e.g., flow depth and velocity) of past debris flows. Yet we acknowledge that this material is more likely coarser grained than the sediments in the tail of such a flow (McArdell et al., 2007). In the laboratory, all of the collected material was processed following the state-of-the-art protocol (SN670 004–2b–NA norm), which was established at the Bern University of Applied Sciences (Burgdorf). Following this protocol, the material was first dried and then sieved to a minimum particle size of 0.5 mm using a set of 7 sieves, each of which has a defined mesh size: 31.5 mm, 16 mm, 8 mm, 4 mm, 2 mm, 1 mm, and 0.5 mm. Subsequently, a slurry analysis was carried out on the material < 0.5 mm using a hydrometer. The goal of this task was to determine the particle size distribution between 0.1 and 0.001 mm. Finally, the grain size distribution of the remining material between 0.5 and 0.063 mm was determined by wet sieving. During this task, we used three sieves where the mesh size was 0.25 mm, 0.125 mm and 0.063 mm. The grain size distribution was truncated at 16 mm so that the entire sample is at least 100 times the mass of the largest particle (e.g., Church et al., 1987). We note, however, that particles larger than 16 mm do occur on the levee deposits and we did sample such material in the field. However, we were not able to consider this fraction due to technical limitations in our laboratory and practical limitations on the mass of the sample necessary for analysis.

Deleted: under the bridge
Deleted: 2c)
Deleted: and dilution
Deleted: The levees were chosen because they
Deleted: considered to
Deleted: grain size
Formatted: Font colour: Auto
Formatted: Font colour: Auto
Deleted: in turn has
Formatted: Font colour: Auto
Formatted: Font colour: Auto
Deleted: potential to determine
Deleted: the
Deleted: (
Formatted: Font colour: Auto
Deleted: . The samples were
Deleted: using
Deleted: methods
Deleted:)
Deleted: Accordingly
Deleted: set of
Deleted: sizes.
Deleted: test

3.4 Powder XRD

We hypothesize that clay minerals influence the pore pressure of a flow (Barshad, 1952), which in turn could influence its mobility (McArdell et al., 2007). We expect such a control because swelling clays tend to absorb water in their crystal structure. The result is an increase in the viscosity of the flow, thereby reducing the dissipation of the fluid pore pressure. To test this hypothesis, the mineralogical properties of some debris flow samples were measured

Deleted: infer
Deleted: influences
Deleted: the

through standard powder XRD at the Institute of Geological Sciences of the University of Bern. For this purpose, four samples were chosen from fast and slow velocity flows as well as from deposits where either the coarse-grained or the fine-grained fractions dominate, in the analyzed grain size spectrum. To this end, the grain size fraction < 0.063 mm, which was already extracted during the steps outlined above, was analyzed for powder XRD. Subsequent milling with a vibrating-disc mill (Retsch RS 200) and a McCrone XRD-mill reduced the particle sizes to the sub-micrometer scale. Corundum powder was added as standard to the samples, and the samples were measured with the x-ray diffractometer X'Pert Pro MPD with Cu radiation. Because this step did not include a determination of the mineralogic composition of the clay minerals, a slightly different approach had to be employed. Here, we used the same initial material, but it was only milled with the vibrating disc mill. The powder was then mixed with a dispersant (0.1 molar NH_3) to achieve a homogeneous suspension. The clay particles were separated in an Atterberg cylinder. The particles still in suspension after 15 hours were extracted using a centrifuge. The extracted clay particles were then cleaned with HCl, $CaCl_2$ and deionized water. To distinguish between the different clay minerals, three sample holders were either air dried, treated with ethylene glycol or heated to 400°C and 550°C before measuring with the X'Pert Pro MPD with Cu radiation. The final processing of the data was carried out with the software TOPAS (Coelho, 2018), which uses a Rietveld structure refinement technique (Rietveld, 1969).

4 Results

4.1 Survey results

A total of 13 events from 2019, 2021, and 2022 were analyzed (Appendix A, Table 1). The measured flow velocities varied by one order of magnitude from 0.89 m/s to 8.69 m/s. The maximum flow depths ranged from 1.13 m to 3.13 m, and the Froude numbers spanned the interval between 0.27 to 2.35, pointing towards considerable differences in the dynamics of these flows. The total volumes reached a maximum of c. 176,000 m^3 and the maximum discharge rate was c. 190 m^3/s. The measured density ranged from 1189 kg/m^3 to 2323 kg/m^3, and the corresponding volumetric water contents were between c. 20% and 90%.

Table 1: Measured and analyzed debris flow events from 2019, 2021, and 2022. Velocity, flow depth, volume, maximum discharge (Qmax) and density are the results of direct measurements at the monitoring station in the Illgraben (Figure 1c). The Froude number was derived from these. The last two columns show, for which events XRD analyses and RAMMS simulations were performed. The event of the 26th of July 2019 could not be simulated due to the high Froude number.

Event date	Velocity [m/s]	Flow depth [m]	Froude number [ ]	Volume [m^3]	Qmax [m^3/s]	Density [kg/m^3]	XRD analysis	RAMMS simulation
21.06.2019	6.62	3.13	1.19	97394	147.61	1870		✓
02.07.2019	3.86	1.75	0.93	73188	65.58	1971	✓	✓
26.07.2019	8.69	1.39	2.35	113310	93.26	2223	✓	

Deleted: diffraction
Deleted: .
Deleted: diffraction
Deleted:
Deleted: to identify the nature and composition of the clay minerals.
Deleted: vary
Deleted: range
Deleted: . Accordingly,
Deleted: range from
Deleted: reach
Deleted: .
Deleted: rates were
Deleted: ranges
Deleted: related
Deleted: .

11.08.2019	6.95	1.81	1.65	88064	95.63	2323		✓
20.08.2019	0.89	1.13	0.27	6137	8.06	2031	✓	✓
24.06.2021	8.18	2.40	1.69	105032	162.20	1750		✓
06.07.2021	8.69	2.50	1.75	76906	186.61	1605		✓
16.07.2021	2.78	2.38	0.58	80879	60.70	1916	✓	✓
07.08.2021	2.32	2.49	0.47	38737	41.19	1884		✓
19.09.2021	1.25	1.13	0.38	8538	10.67	1697		✓
05.06.2022	3.39	2.08	0.75	39498	55.42	1690		✓
04.07.2022	8.18	2.49	1.66	175929	169.14	1189		✓
08.09.2022	1.91	1.93	0.44	9283	20.94	1592		✓

4.2 Numerical modelling with RAMMS

As mentioned above, we iteratively changed the μ– and ξ–friction values upon modelling until we found a best-fit between the modelled and observed flow velocity and flow depth of each flow (Appendix C and D). Because the latter properties of a debris flow (velocity and depth) can be characterized by the Froude number (defined by eq. (2)), we first describe the dependency of the modelled flow pattern on the Froude number, which itself is calculated using the flow depth and velocity data of the field survey (Table 1). Please note that in this context, eq. (2) predicts that changes in the flow velocity have a larger impact on the Froude number than variations in flow depth. The simulations showed that RAMMS produces reasonable results (e.g., Figure 2) for Froude numbers up to about 1.75 (Table 1). For larger values (e.g., flows with large flow velocities), the simulations predict the occurrence of standing waves at the debris flow front, which, however, have not been observed at the Illgraben. Therefore, no simulations were possible for the event on the 26th of July 2019, because this flow was characterized by a Froude number of 2.35. We acknowledge that roll-waves, which could correspond to the standing waves simulated by RAMMS, do occur in a debris flow, but such waves are mainly observed in the debris flow body and not at the bouldery front.

Deleted: Because the main output parameters from

Deleted: RAMMS simulations (Appendix B) were

Deleted: (Figure 3),

Deleted:) proved to be useful for characterizing these flows.…

Deleted: equation *(2)*

Deleted: .

Deleted: during this study. Flows with large Froude numbers tend to be characterized by roll-waves, which may correspond to the predicted standing waves by RAMMS…

Deleted: Also, the occurrence of

Deleted: be

Deleted: some real

Deleted: flows, could

Deleted: be modeled with RAMMS.

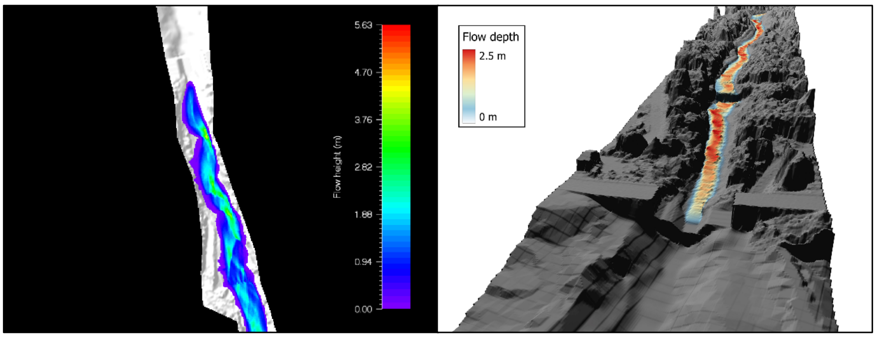

Figure 2: Example of simulated flow depths. The image on the left shows flow depths in a 2D view provided by the RAMMS software. The image on the right shows a 3D view of the debris flow projected on a hillshade model using the QGIS software.

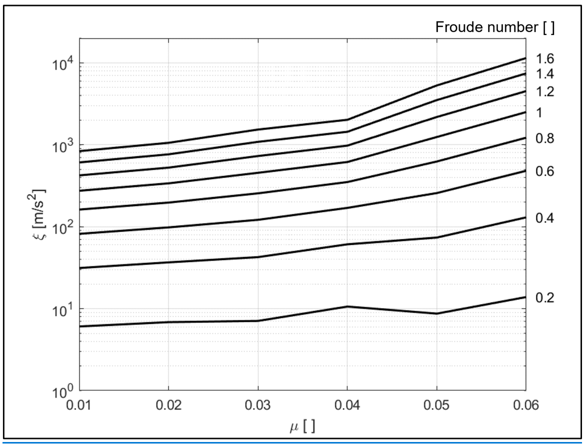

Figure 3: Modelled μ–ξ pairs, which result in a best fit between the observed and the modelled debris flow parameters. These latter values, in turn, appear to depend on the Froude numbers (based on measurements in the field, see Table 1) of the corresponding debris flow events.

The model results show that more than one best-fit μ–ξ pair is possible for successfully reproducing the observed velocity and depth of a flow (Appendix E). Yet, on average, the lowest *z*-value is calculated for the μ–ξ pair with μ = 0.01, followed by the pairs with μ = 0.02 and μ = 0.05. These values and patterns are consistent with the results of other debris flows analyses conducted with RAMMS and applied to observations in e.g., the Alps (see Mikoš and Bezak, 2021, for an overview of related papers), the Himalayas near Luzhuang in China (Jianjun and Zhang; μ– and ξ–values of 0.07 and 1500 m/s^2), and the coastal region in the vicinity of Western Ghats in India (Abraham et al., 2021; μ– and ξ–values of 0.01 and 100 m/s^2, respectively). In addition, Simoni et al. (2012) found that RAMMS successfully reproduced the maximum observed runout distances of debris flows in the Italian Alps for μ–

Deleted: 3

Deleted: . The μ–ξ pair with μ = 0.01 has

Deleted: These

values close to the energy gradient of the debris flow channel (which is the tangent of the surface slope). Our modelling results support these inferences and additionally show that the modelled μ– and ξ–relationships show a strong dependency on the corresponding Froude numbers calculated from the field data (Figure 3, and Appendix E, F). Besides, for a given μ–value, the RAMMS models predict that the ξ–values increase with the Froude number. Such an increase is more obvious for large than for small μ–values (Figure 3, see also Appendix F).

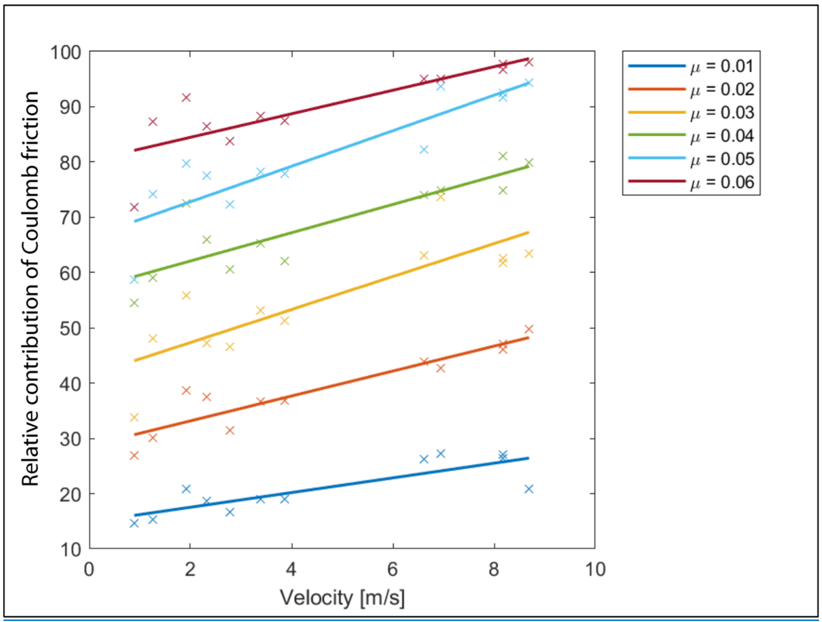

Figure 4: Correlations between the relative contribution of the Coulomb friction to the total friction in percent (y-axis) and the velocity of a debris flow (x-axis) for different μ-values. The data points refer to best-fit simulations only. The lines are first order polynomial least square fitted trendlines.

Figure 4 illustrates that upon modelling, the relative contribution of the Coulomb friction to the total friction increases with the flow velocity, and it shows that this contribution is greater for large μ-values than for small ones. In particular, while the percentages of the Coulomb friction are in the range of c. 20% for a μ-value of 0.01 and a flow velocity of < 1 m/s, they increase to > 90% for a larger μ-value of 0.06 and a flow velocity of > 8 m/s.

Deleted: also

Deleted: (

Deleted:).

Formatted: Caption, Left, Line spacing: single

Deleted: ¶

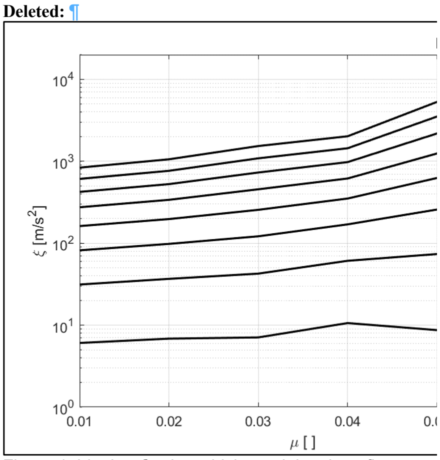

Figure 4: Ideal μ–ξ pairs, which result in a best fit between the observed and the modelled debris flow parameters, which, in turn, appear to depend on the Froude numbers of the corresponding debris flow events. ¶

¶

The total friction S is the sum of a basal friction component that is scaled by μ, and an internal friction contribution, which in turn depends on ξ (see above). Figure 5 shows the absolute values of the friction components as a function of the selected μ-value. Debris flows dominated by basal friction (large μ) tend to appear more turbulent on the video recordings.

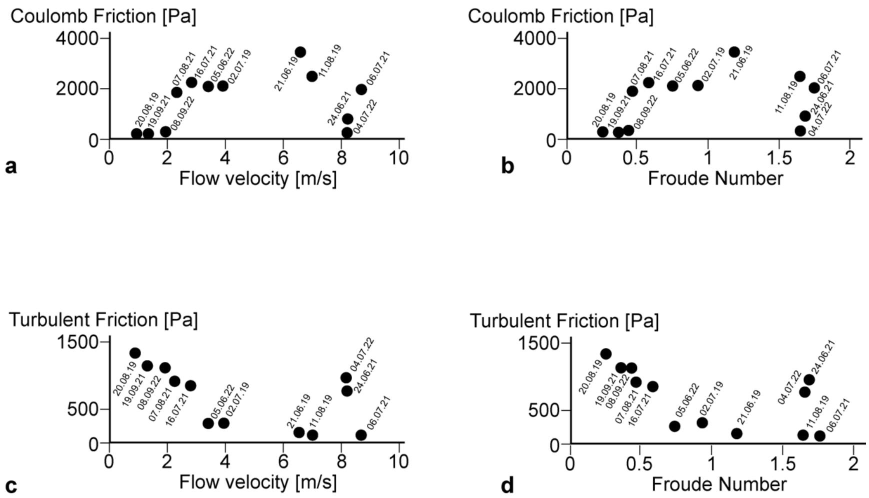

Figure 5: Relationships between a) flow velocity and Coulomb friction, b) Froude number and Coulomb friction, c) flow velocity and turbulent friction, and d) Froude number and turbulent friction. The plots show the results of the best-fit simulations for each flow.

The relationships elaborated above are further detailed in Figure 5, which documents the dependency of the friction property (Coulomb and turbulent friction) of a flow on its velocity and the corresponding Froude number. Note that for this analysis, we only considered the results of the best-fit simulations of each flow. Accordingly, rapid debris flows with high Froude numbers tend to be characterized by a large Coulomb friction, while slower debris flows are simulated more reliably with a rather low Coulomb friction (Figures 5a, 5b). Conversely, flows with a slow velocity tend to have a larger turbulent friction and are characterized by a low Froude number, whereas the turbulent friction tends to be low for flows with a high velocity and a high Froude number (Figures 5c, 5d). However, we note that the aforementioned relationships between flow velocity, Froude number, turbulent and Coulomb friction break down for flows that are more rapid than c. 6-7 m/s (Figure 5). Similar to the event on 26th of July 2019, these flows are characterized by Froude numbers that are much larger than 1 (Table 1). These flows appear to be in a condition in which the relationships between friction and flow properties are apparently non-linear and more complex than in flows, which can be characterized by low Froude numbers. A further elaboration of this topic is, however, beyond the scope of this paper.

Figure 6 summarizes the consequences of the aforementioned relationships. In particular, small values of the Coulomb friction coefficient (μ ~ 0.01), when the flow is moving on the order of a few meters per second, indicate that the contribution of the Coulomb term to the total friction is small, and that the total friction is therefore dominated by the turbulent friction term (Figure 6). In the extreme case when μ = 0, the turbulent friction term (eq. 1) closely resembles a Chezy friction from open-channel hydraulics (e.g. Henderson, 1966). Large values of the Coulomb friction coefficient (here μ ~ 0.05) suggest that the Coulomb friction term is important, and that the contribution of the turbulent friction is correspondingly less significant (Figure 6). Because we found ideal μ–ξ pairs with μ = 0.01–0.02 and μ = 0.05 for most debris flows, we considered these flows to be dominated either by (i) the turbulent friction (flows with μ = 0.01–0.02) or by (ii) the Coulomb friction (flows with μ = 0.05). Note that Figure 6 also shows that the total friction S increases with a larger μ. Nevertheless, the output of the simulation (velocity and flow depth) is similar regardless of which μ–ξ pair variant is chosen.

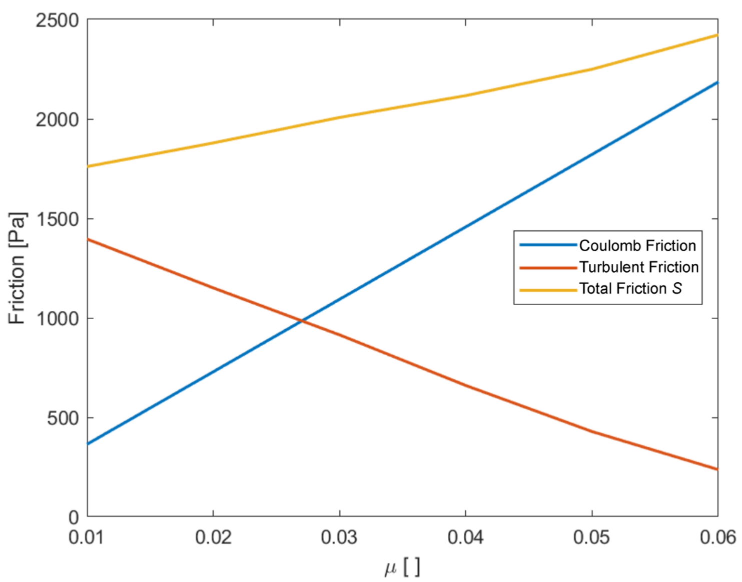

Figure 6: Values of Coulomb friction, turbulent friction, and total friction S as a function of the selected Coulomb friction coefficient μ. The plotted values are averages of the friction magnitudes of all best-fit simulations. The blue line represents the Coulomb friction contribution. The red line is the turbulent friction, and the yellow line is the total friction.

4.3 Grain size distribution

Samples from 14 debris flows were analyzed for their grain size distribution (Figure 7 and Appendix G). Note that there was a sediment sample but no monitoring data for the event on the 4th of October 2021. All events show a very similar grain size distribution. An exception, and thus an outlier, is a sediment sample that has a larger relative abundance of fine-grained material. This sample was taken from a debris flow, which occurred on the 2nd of July 2019. For all samples, the clay fraction has a relative mass abundance of 2–3%, the silt fraction 27–

35%, the sand fraction 27–40% and the part of the gravel fraction that is covered by the analysis 23–37%. Note that the gravel fraction >16 mm was also analyzed (Appendix G). Yet we normalized the grain size data to 16 mm, because it was not feasible to collect larger mass-representative samples. Therefore, we acknowledge that the upper percentiles are affected and thus biased by this cut-off and the related percentage values have to be considered with caution.

For all samples, we measured grain sizes of 0.015–0.02 mm for the 16% percentile, 4–9 mm for the 84% percentile and 10–15 mm for the 95% percentile. The median grain size ranges from 0.15 mm to 0.5 mm. In general, the material was very poorly sorted with a skewness towards the fine-grained fraction. Interestingly, the grain size distribution was quite similar for all sampled material. Based on the available datasets, we are neither able to determine whether the mean grain size is more variable in space than in time, nor can we detect whether the coarse-grained fraction (>16 mm) could be highly variable whereas the fine-grained material is more homogeneous. However, similar to the mineralogical composition, which is also quite similar between the various flows, we interpret that the rather homogeneous granulometric composition at least of the fine-grained portion of the sediment is the direct consequence of the cascade of sediment mixing in the upstream part of the Illgraben (Schlunegger et al., 2009).

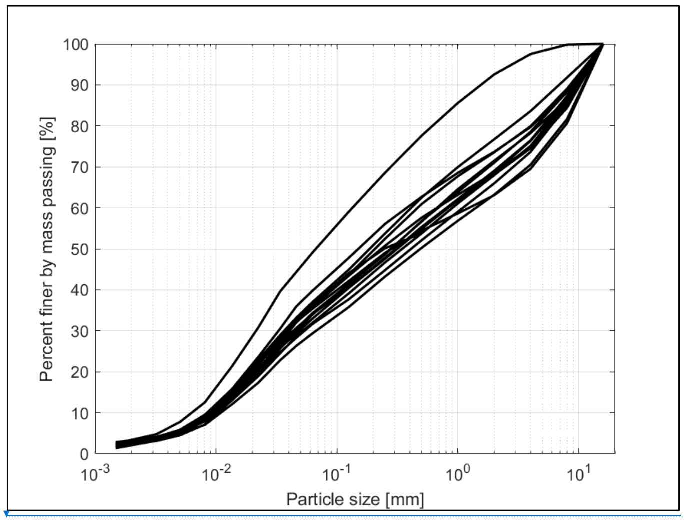

Figure 7: Diagram showing the grain size distribution of all 14 sampled debris flow deposits, truncated at a maximum grain size of 16 mm.

Deleted: just recorded up to a

Deleted: of

Deleted: We

Deleted:

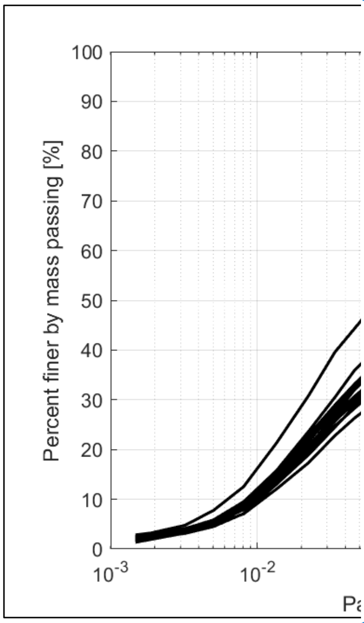

Deleted: 6

Deleted: calibrated to

4.4 Powder XRD

The results of the powder XRD analysis (Appendix H) show that quartz was the main mineral of the silt fraction and contributes between 29 and 36 wt% (Figure 8). In addition, dolomite (17–24 wt%), muscovite (18–22 wt%), calcite (7–18 wt%) and illite minerals (8–12 wt%) are present in all samples. Feldspar grains occur by < 5 wt%, and the clay minerals chlorite, kaolinite and smectite are present in small quantities (< 1%) or are below the detection limit. Calcite shows the greatest variation in the mineralogical composition with differences up to 11 wt%. The other main components including quartz, dolomite, muscovite and illite show variations with a maximum of 7 wt%. The feldspar minerals albite and orthoclase are very homogeneously distributed in the four samples. Overall, the variations in the mineralogical composition between the different samples are only minor and often lie within the methodological error of ± 10% of the measured values. Yet, some albeit minor differences can be detected when the compositions of the coarse- and fine-grained samples are compared. In the coarse-grained sample, calcite crystals are more abundant than in the sample characterizing a fine-grained debris flow. In contrast, the latter sample has a larger relative abundance of illite minerals than the sample made up of coarser sediments. Although the database is sparse, we tentatively consider these differences to reflect a source signal where the heavily fractured basement rocks and Triassic schists, which also host the illite crystals, have the potential to supply larger volumes of fine-grained material than the bedrock made up of limestones.

From the clay minerals, only smectite can absorb larger amounts of water (Likos and Lu, 2002). However, the x-ray spectra of muscovite and smectite crystals cannot be distinguished with the applied XRD method. Because the basement rocks and the Triassic schists are considered to be the source of the clay minerals in the catchment area (Schlunegger et al., 2009), the signal is more likely related to the fine-grained muscovite (sericite) than to the smectite minerals (Scheiber et al., 2013). Therefore, swelling clay minerals are expected to be of minor importance in this case.

Deleted: D

Deleted: 7

Deleted: measured

Deleted: &

Deleted: .

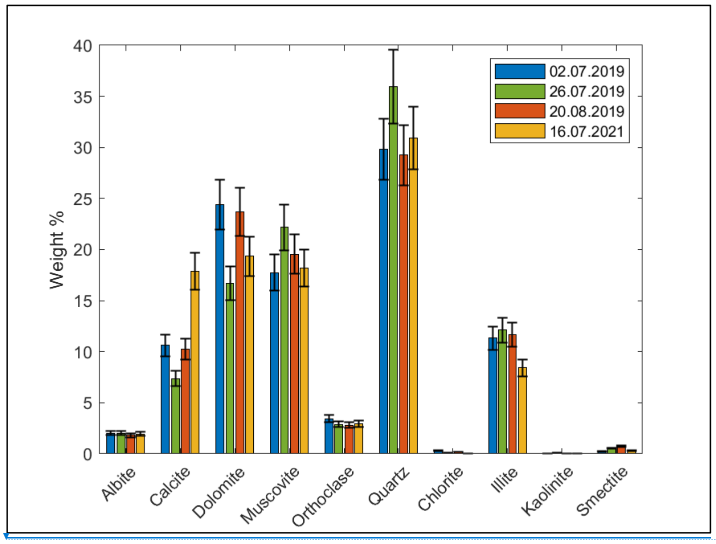

Figure 8: Mineralogic composition of four samples analyzed by powder-XRD. The black error bars indicate a methodological error of 10% of the measured value. The material representing the flow on the 2nd of July 2019 was exceptionally fine-grained (Appendix G); the flow on the 26th of July of the same year was an event with a high velocity (8.69 m/s), and it was the most rapid flow (Table 1). The debris flow on the 20th of August, again in 2019, was very slow (0.89 m/s) and it was indeed the slowest flow during the survey period (Table 1). The material taken from the debris flow on the 16th of July 2021 was characterized by a rather coarse-grained matrix (Appendix G).

4.5 Statistical evaluation of the debris flow properties

A statistical evaluation of the debris flow parameters measured at the monitoring station shows a positive correlation between velocity, flow depth, volume, and maximum discharge (Figure 9). While velocity, volume, and maximum discharge correlate very strongly among themselves as they are physically related (auto-correlation), the correlation of these parameters with the flow depth is less evident, yet a weak positive correlation is certainly visible. Accordingly, and as expected (McArdell et al., 2003), a debris flow with a large volume tends to have a large flow velocity and flow depth, which consequently also results in a large maximum discharge and a large Froude number. On the other hand, debris flows that have a small volume are also slow, and they have both a small flow depth and a low Froude number. Interestingly, clear correlations between grain size, clay content and flow properties are not visible in our analyses (Figure 10). Also, no correlation between the inferred water content and the volume or maximum discharge was found for these events. Yet, the total friction values that are extracted from the modelling results tend to show a positive correlation with the flow depth, and a weak positive correlation with the density and thus the water content (Figure 9).

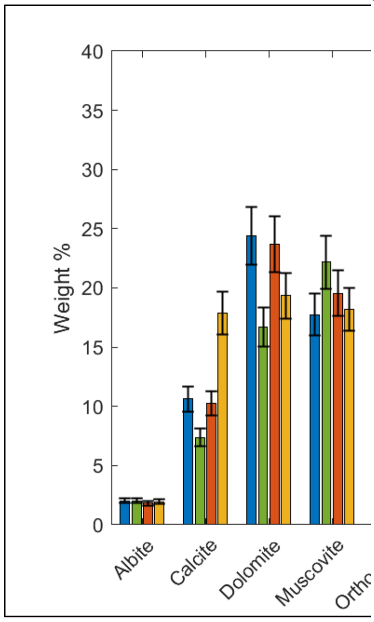

Deleted:

Deleted: 7

Deleted: ;

Deleted:).

Deleted: flows

Deleted:), and that

Deleted: 1st

Deleted: August

Deleted: .

Deleted: of the debris flows

Deleted: 8

Deleted: As expected, the values of the Froude number correlate positively and strongly with the velocity (auto-correlation) and also positively with the volume and the maximum discharge of the flows. No correlation can be found between the Froude number values and the flow depths, which illustrates the dominance of the velocity on the Froude number in our case. If just the volume of the sediment load is considered, the correlations become less strong for most of the parameters. Yet, positive correlations between this variable and the flow velocity, and especially with the Froude number, are apparent. Interestingly, correlations between grain size, clay content and flow properties are not apparent in our analyses (Figure 9).¶
In summary,

Deleted: In addition

Deleted: clear

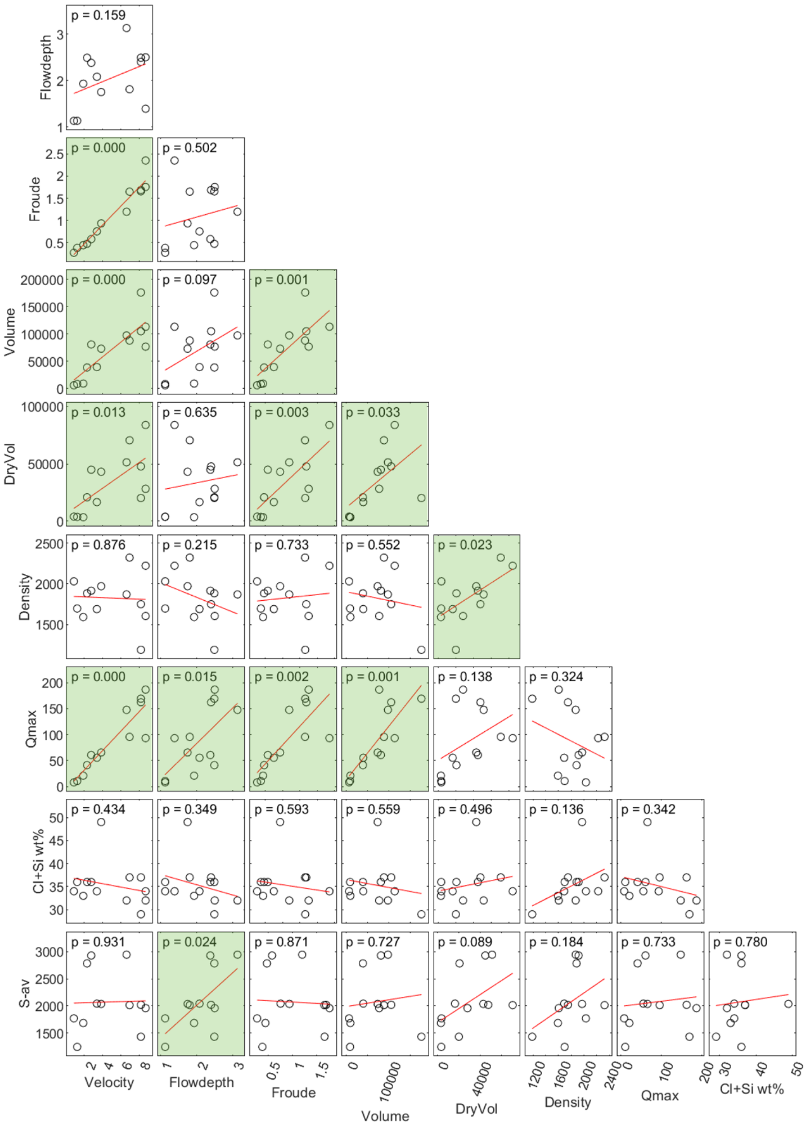

Figure 9: Statistical correlations between dynamic properties of the debris flows with a statistical p-value. For correlation tests a significance level of 0.05 is considered. Correlations with p-values < 0.05 can therefore be considered as significant (illustrated with green color). Measurements from the monitoring station at the Illgraben and values derived from them are front velocity [m/s], maximum flow depth [m], Froude number [ ], total volume [m^3], dry sediment volume [m^3], density of a flow [kg/m^3], which points to the water content and the maximum

Deleted:

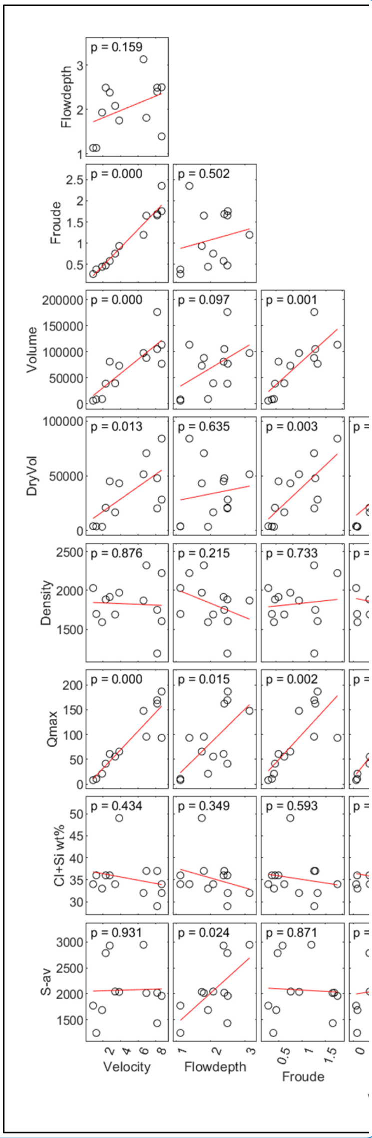

Deleted: 8

Deleted: values8

Deleted: .

discharge [m^3/s]. From the grain size analyses, we have the percentage of the sum of clay and silt in the sample [wt%]. From the modelling with RAMMS we get the total amount of friction [Pa] as average of all best-fit simulations of a certain event. The plots were generated using a modified version of the Correlation Matrix Scatterplot by Chow (2022), for MATLAB. Note that a statistical p-value with p = 0.000 means that the value is less than 0.0005, and therefore it is rounded down to 0.

Deleted: modeling
Deleted: accomplished
Deleted: designed
Formatted: Font colour: Black

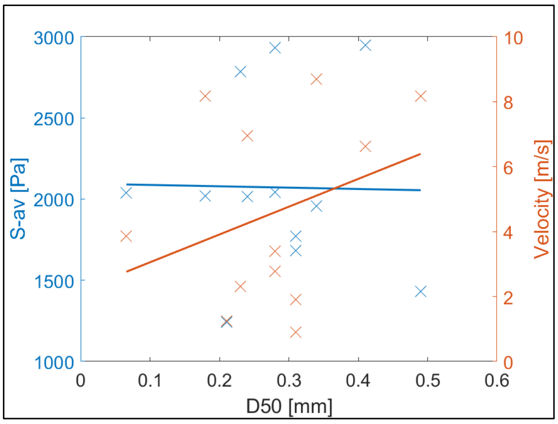

Figure 10: Correlation (first order polynomial trendlines accomplished by least square fitting) between the total amount of friction S-av as average of all best-fit simulations of a certain event and the D50 value of the corresponding sediment sample (blue), and correlation between the measured velocity of the flow and the D50 value of the corresponding sediment sample (red).

Deleted: 9

5 Discussion

The debris flows observed in the years 2019, 2021 and 2022 show large differences in their dynamics, where flow depths and flow velocities varied by a factor of 3 and 10, respectively. Despite these variabilities in the surveyed parameters, most of the flows could be simulated with RAMMS, and the model outputs yielded consistent results regarding the underlying controls and the simulated flow kinematics and properties (see Appendix C, D, E and F, and the related z-values). In the following section, we discuss how the various parameters such as the grain size and mineralogical distribution of the fined-grained matrix as well as the friction properties potentially exerted a control on the surveyed debris flows.

Deleted: registered
Deleted: even
Deleted: .

5.1 Relationships between volume, flow velocity and flow depth, and controls on friction properties

The statistical tests show positive correlations between volume, flow velocity, flow depth and maximum discharge rate. Our results are thus consistent with similar results reported by Rickenmann (1999), de Haas et al. (2015) and Hürlimann et al. (2015) and reflect the open-channel hydraulic principles used to compute these parameters (McArdell et al., 2023). Indeed, as shown by the aforementioned authors, flows with larger volumes may contain a larger number of pebbles and boulders, which according to Johnson et al. (2012) are likely to

Deleted: .
Deleted: probably

accumulate on the front of these flows. As a result, the frictional resistance of the frontal part increases (Iverson, 1997), with the consequence of a damming effect such as that the flow depths will increase. We indeed see such a mechanism at work in the surveyed flows through positive correlations between flow depth, flow velocity and flow volume. We thus infer that the volume can be considered as the most important driving parameter for explaining the debris flow dynamics in the Illgraben system and therefore can be considered as a key parameter. This confirms standard practice in hazard analysis, which gives primary importance to event volume. We note that this argument relies on the debris flows all having the same initial grain size distribution, which, as discussed above, we can only document for sediment sizes smaller than 16 mm. Yet, we acknowledge that a visual comparison of the videos (Appendix B) clearly shows differences in the abundance of relatively coarse sediment (e.g., boulders). A more detailed analysis on this topic will require additional data and is beyond the scope of this paper. The evaluation of the RAMMS simulations shows that there are several μ–ξ pairs, which yield ideal solutions upon simulating the surveyed debris flows. In particular, the same flow can successfully be reproduced by RAMMS with large and low Voellmy μ–values. However, an assessment of which of these possibilities is more appropriate can be found if the flow velocity is used as a criterion. Indeed, our analysis showed that debris flows with a high velocity (up to 6-7 m/s) tend to be dominated by a large Coulomb friction (large μ–value), whereas flows with a low velocity have a low Coulomb friction (low μ–value) but a relatively high turbulent friction (Figure 5). Yet for flows with velocities that are larger than 6-7 m/s, these relatively simple relationships break down most likely because such flows appear to be in a condition where the flow pattern is more complex (e.g., roll waves with Froude numbers that are much larger than 1 to 1.5, Table 1).

We note that while it is tempting to interpret such low– μ flows as being 'laminar' and large– μ flows as 'turbulent' (because of the low and high Froude numbers, see also Figure 5), independent criteria for determining the presence or absence of turbulence in debris flows are not yet available. A hydraulics-based estimate based on the Reynolds number to characterize the presence or absence of turbulence (e.g. Henderson, 1966) requires estimates of the rheology of the entire flow, which are not available. In addition, it is unclear to what extent rheological measurements of fine sediment slurries can represent the overall viscosity of the flow given the presence of other processes such as the jamming of particles in the flow (Kostynic et al., 2022). Yet, such calculations are beyond the scope of this contribution.

5.2 Influence of the grain size distribution and mineralogy

The granulometric analysis of the levee deposits indicates a rather homogeneous grain size distribution for the clay, silt, sand and the fine-grained gravel fraction. The grain size distribution fits quite well with the granulometric analyses of the debris flow deposits at the

Deleted: mechanisms

Deleted: to reliably simulate a given event

Deleted: known properties. In detail, the flows can be interpretated

Deleted: basal

Deleted: Voellmy μ values) or dominated by internal

Deleted: Voellmy ξ values, which yields a large internal

Deleted: according to equation *1*). We speculate that which of these two solutions is more accurate

Deleted: a given event could possibly be determined by measuring the internal distribution of the flow

Deleted: . Large and variable internal flow velocities could be attributed

Deleted: occurrence

Deleted: would thus be consistent with a low internal friction, but a large basal friction. Alternatively, a flow with a more homogeneous distribution of internal velocities is more likely to indicate the occurrence of less turbulent (or possibly laminar) flow where viscous shear forces and thus a high internal friction dominate

Deleted: friction (e.g., Figure 5).

Illgraben published by Hürlimann et al. (2003). Because of a lack of correlations between the relative proportion of the fine fraction to the parameters that characterize the flow properties (e.g., friction and flow velocity; Figure 10), the variations in the dynamics of these flows cannot be simply explained by a simple fixed friction relation such as in the Voellmy relation. This inference is consistent with the notion by Iverson (2003) who states that the evolution of debris flow behavior upstream of the front is likely to be complex. In the same sense, because of the homogeneity of the samples with respect to the grain size distribution of the components smaller than 16 mm, also the relative abundance of the sand to the fine-grained gravel fraction cannot be related to variations in the flow dynamics. Nevertheless, an influence of the grain size composition on the debris flow dynamics, as described by de Haas et al. (2015) and Hürlimann et al. (2015), cannot be fully excluded, (see section 1.1). Because the relative abundances of the different fractions are similar, their potential influence on the flow properties should also be similar for each event. Due to this similarity, such relationships (if present) would not be detectable with the measurements presented herein. Admittedly, we also have no information to exclude a potential control of the coarse-grained fraction such as coarse gravel, cobbles, and boulders, on the flow dynamics, as described by de Haas et al. (2015). Attempts to reconstruct the full grain size distribution are hampered by a lack of information on the grain size below the surface of the flow (e.g., Uchida et al., 2021). In addition, the influence of small changes of the topography on the results was not investigated here, but could improve the correlations of the flow properties to grain size if adequately considered.

Similar to the grain size distribution of the fine-grained matrix, we do not see a relationship between the mineralogical composition of the matrix and the flow properties. Among the various minerals that are present in the debris flow deposits (Appendix H), we expect to see a control of the sheet silicates on the velocity of the flows, mainly because clay minerals and particularly smectite-type of clays have the potential to absorb water in their crystal structure (see section 1.1). We therefore expect that a high relative abundance of such minerals will alter the flow rheology and particularly the flows' turbulent friction, which is expected to impact the flow velocity. Apparently, this is not the case at the Illgraben. We consider this absence of relationships to reflect a supply signal, because the relative abundance of swelling minerals is negligible in the source area where other sheet silicates such as illite and muscovite crystals predominate (Scheiber et al., 2013). These silicates don't have swelling properties and apparently do not impact the velocity of the debris flows at the Illgraben. However, the homogeneity in terms of the mineral composition and also the grain size composition between the samples confirms the results of previous studies that inferred the occurrence of an efficient mixing mechanism as the material is transferred from the source area to the Rhone River (Schlunegger et al., 2009; Berger et al., 2011a).

Deleted: 9

Deleted: and even

Deleted: .

Deleted: exerted by

Deleted: in the Illgraben

Conclusion

The results obtained in the Illgraben system by comparing various debris flow parameters with data from runout modelling, grain size analyses, XRD analyses can be summarized as follows:

1) The simulation of debris flows with RAMMS yields multiple solutions with different friction coefficients μ and ξ in the Voellmy equation. The resulting Coulomb and turbulent friction are correlated with the Froude number and runout velocity of the debris flow yet only as long as the flow velocity is < 6-7 m/s.
2) The dynamics of a debris flow in the Illgraben (i.e., flow velocity and flow depth) is strongly dependent on its volume. If information about the sediment volume in the source area is available, the parameters for simulating a potentially worst-case debris flow and its impact can theoretically be assessed with some uncertainties.
3) Due to the relatively large homogeneity of the deposits with respect to the grain size distribution and the mineralogical composition, an efficient mixing process in the Illgraben can be inferred.
4) Based on these data, variations in the dynamics of different debris flows cannot be attributed to the grain size distributions of the clay, silt, sand or fine-grained gravel fractions. Consequently, an assessment of a potential debris flow or a definition of a simulation based on grain size compositions in the source area is not possible in the case presented here.

Such relationships are particularly useful for the assessment of natural hazards, as they provide specific evidence for the estimation of a debris flow and its impact.

Acknowledgement

We are grateful for the technical support provided by Franziska Nyffenegger (grain size analysis), Pierre Lanari and Michael Schwenk (statistics) as well as Frank Gfeller and Anulekha Prasad (XRD analysis). We thank the WSL staff for their support with sampling and the support of Marc Christen and Perry Bartelt (RAMMS) is greatly appreciated.

Data availability

All data used in this paper are listed in Table 1 and in the supplementary files.

Autor contributions

BM and FS designed the study. DB conducted the experiments, collected the data and processed the samples. DB wrote the paper, with contributions by FS and BM. All authors discussed the article.

Competing interests

Deleted: ratios, all of which lead to quite similar results. The …

Deleted: , which are responsible for the scaling of the friction terms…

Deleted: , can be estimated from

Deleted: adequate

Deleted: .

Deleted: FS

Deleted: BM

The authors declare that they have no conflict of interest.

References

Abraham, M.T., Satyam, N., Peddholla Reddy, S.K., and Pradhan, B.: Runout modeling and calibration of friction parameters of Kurichermala debris flow, India. Landslides, 18, 737-754. https://doi.org/10.1007/s10346-020-01540-1.

Allen, P. A.: Earth surface processes. Blackwell Science, 1997.

Badoux, A., Graf, C., Rhyner, J., Kuntner, R., and McArdell, B. W.: A debris-flow alarm system for the Alpine Illgraben catchment: Design and performance, Nat. Hazards, 49, 517–539, 2007. https://doi.org/10.1007/S11069-008-9303-X/FIGURES/7

Barshad, I.: Absorptive and swelling properties of clay-water system, Clays Clay Miner., 1(1), 70–77, 1952.

Bartelt, P., Valero, C. V., Feistl, T., Christen, M., Bühler, Y., and Buser, O.: Modelling cohesion in snow avalanche flow, J. Glaciol., 61, 837–850, 2015. https://doi.org/10.3189/2015JoG14J126

Belli, G., Walter, F., McArdell, B., Gheri, D., and Marchetti, E.: Infrasonic and Seismic Analysis of Debris-Flow Events at Illgraben (Switzerland): Relating Signal Features to Flow Parameters and to the Seismo-Acoustic Source Mechanism, J. Geophys. Res. Earth, 127, e2021JF006576, 2022. https://doi.org/10.1029/2021JF006576

Bennett, G. L., Molnar, P., McArdell, B. W., Schlunegger, F., and Burlando, P.: Patterns and controls of sediment production, transfer and yield in the Illgraben, Geomorphology, 188, 68–82, 2013. https://doi.org/10.1016/j.geomorph.2012.11.029

Berger, C., Christen, M., Speerli, J., Lauber, G., Ulrich, M., And McArdell, B. W.: A comparison of physical and computer-based debris flow modelling of a deflection structure at Illgraben, Switzerland, Data Acquisition and Modelling (Monitoring, Processes, Technologies, Models), 212–220, 2016.

Berger, C., McArdell, B. W., Fritschi, B., and Schlunegger, F.: A novel method for measuring the timing of bed erosion during debris flows and floods, Water Res. Res., 46, 2010. https://doi.org/10.1029/2009WR007993

Berger, C., McArdell, B. W., & Schlunegger, F.: Sediment transfer patterns at the Illgraben catchment, Switzerland: Implications for the time scales of debris flow activities, Geomorphology, 125, 2011a. 421–432. https://doi.org/10.1016/j.geomorph.2010.10.019

Berger, C., McArdell, B. W., and Schlunegger, F.: Direct measurement of channel erosion by debris flows, Illgraben, Switzerland, J. Geophys. Res., 116, 2011b. https://doi.org/10.1029/2010JF001722

Formatted: Indent: Left: 0.85 cm, Hanging: 1 cm

Bumann, N.: Effect of Geological Preconditioning on Sediment Production in the Illgraben Catchment [Ms thesis]. University of Bern, 2022.

Chatterji, P.K., and Morgestern, N.R., 1990. A modified shear strength formulation for swelling clay soils. In: Proc. Symp. Physico-Chemical Aspects of Soil, Rock and Related Materials, St. Louis. ASTM Spec. Tech. Publ. N1095, 118-139.

Choi, C. E., Ng, C. W. W., Au-Yeung, S. C. H., and Goodwin, G. R.: Froude characteristics of both dense granular and water flows in flume modelling, Landslides, 12, 1197–1206, 2015. https://doi.org/10.1007/S10346-015-0628-8/FIGURES/11

Chow, J. : Correlation Matrix Scatterplot, 2022. https://www.mathworks.com/matlabcentral/fileexchange/53043-correlation-matrix-scatterplot

Christen, M., Bühler, Y., Bartelt, P., Leine, R., Glover, J., Schweizer, A., Graf, C., McArdell, B. W., Gerber, W., Deubelbeiss, Y., Feistl, T., and Volkwein, A.: Integral hazard management using a unified software environment numerical simulation tool “RAMMS” for gravitational natural hazards, 2012. www.interpraevent.at

Church, M., McLean, D., and Wolcott, J.: River bed gravels : sampling and analysis, Sediment Transport in Gravel-Bed Rivers, 43–88, 1987. https://cir.nii.ac.jp/crid/1572261549037050368.bib?lang=en

Coelho, A. A.: TOPAS and TOPAS-Academic: An optimization program integrating computer algebra and crystallographic objects written in C++, J. Applied Crystall., 51, 210–218, 2018. https://doi.org/10.1107/S1600576718000183

de Haas, T., Braat, L., Leuven, J. R. F. W., Lokhorst, I. R., and Kleinhans, M. G.: Effects of debris flow composition on runout, depositional mechanisms, and deposit morphology in laboratory experiments, J. Geophys. Res. Earth Surface, 120, 1949–1972, 2015. https://doi.org/10.1002/2015JF003525

de Haas, T., McArdell, B. W., Nijland, W., Åberg, A. S., Hirschberg, J., and Huguenin, P.: Flow and Bed Conditions Jointly Control Debris-Flow Erosion and Bulking. Geophys. Res. Lett., 49, e2021GL097611, 2022. https://doi.org/10.1029/2021GL097611

Deubelbeiss, Y., and Graf, C.: Two different starting conditions in numerical debris-flow models - Case study at Dorfbach, Randa (Valais, Switzerland). Jahrestagung Der Schweizerischen Geomorphologischen Gesellschaft, 2011.

Di Maio, C.: Exposure of bentonite to salt solution: osmotic and mechanical effects. Géotechnique XLVI (4), 695–707, 1996.

Formatted: Indent: Left: 0.85 cm, Hanging: 1 cm

Formatted: English (US)

Deleted: Mcardell

Formatted: English (US)

Formatted: German (Switzerland)

Di Maio, C., Santoli, L., and Schiavone, P.: Volume change behaviour of clays: the influence of mineral composition, pore fluid composition and stress state. Mechanics Mat., 36, 435-451, 2004. https://doi.org/19.1016/S0167-6636(03)00070-X

Frank, F., McArdell, B. W., Huggel, C., and Vieli, A.: The importance of entrainment and bulking on debris flow runout modeling: examples from the Swiss Alps, Nat. Hazards Earth Sys. Sci., 15, 2569-2583, 2015, https://doi.org/10.5194/nhess-15-2569-2015;

Frank, F., McArdell, B. W., Oggier, N., Baer, P., Christen, M., and Vieli, A.: Debris-flow modeling at Meretschibach and Bondasca catchments, Switzerland: sensitivity testing of field-data-based entrainment model, Nat. Hazards Earth Sys. Sci., 17, 801-815, 2017. https://doi.org/10.5194/nhess-17-801-2017

Gabus, J. H., Weidmann, M., Sartori, M., and Burri M.: Blatt 1287 Sierrre - Geologischer Atlas der Schweiz 1:25 000, Erläuterungen, Bundesamt für Landestopografie swisstopo, 2008.

Henderson, F.M.: Open Channel flow. New York, MacMililan, 1966.

Hirschberg, J., Badoux, A., McArdell, B. W., Leonarduzzi, E., and Molnar, P.: Evaluating methods for debris-flow prediction based on rainfall in an Alpine catchment, Nat. Hazards Earth Sys. Sci., 21, 2773–2789, 2021. https://doi.org/10.5194/NHESS-21-2773-2021

Hirschberg, J., Fatichi, S., Bennett, G. L., McArdell, B. W., Peleg, N., Lane, S. N., Schlunegger, F., and Molnar, P.: Climate Change Impacts on Sediment Yield and Debris-Flow Activity in an Alpine Catchment, J. Geophys. Res. Earth Surface, 126, e2020JF005739, 2021. https://doi.org/10.1029/2020JF005739

Hirschberg, J., McArdell, B. W., Badoux, A., and Molnar, P.: Analysis of rainfall and runoff for debris flows at the Illgraben catchment, Switzerland. Debris-Flow Hazards Mitigation: Mechanics, Monitoring, Modeling, and Assessment - Proceedings of the 7th International Conference on Debris-Flow Hazards Mitigation, 693–700, 2019.

Hübl, J., Suda, J., Proske, D., Kaitna, R., and Scheidl, C.: Debris Flow Impact Estimation, International Symposium on Water Management and Hydraulic Engineering, 137–148, 2009. https://www.researchgate.net/publication/258550978

Hürlimann, M., McArdell, B. W., and Rickli, C.: Field and laboratory analysis of the runout characteristics of hillslope debris flows in Switzerland, Geomorphology, 232, 20–32, 2015. https://doi.org/10.1016/J.GEOMORPH.2014.11.030

Hürlimann, M., Rickenmann, D., and Graf, C.: Field and monitoring data of debris-flow events in the Swiss Alps, Can. Geotech. J., 40, 161–175, 2003. https://doi.org/10.1139/t02-087

Formatted: Normal, Indent: Left: 0.85 cm, Hanging: 1 cm, Don't adjust space between Latin and Asian text, Don't adjust space between Asian text and numbers

Formatted: Default Paragraph Font

Field Code Changed

Formatted: Indent: Left: 0.85 cm, Hanging: 1 cm

Formatted: Indent: Left: 0.85 cm, Hanging: 1 cm

Iverson, R. M.: The physics of debris flows, Rev. Geophys., 35, 245–296, 1997. https://doi.org/10.1029/97RG00426

Jianjun, Z., Zhang, Y.X.: Numerical simulation of debris flow runout using Ramms: a case study of Luzhuang Gully in China. Computer modeling in Engineering & Science, 121, 981-1009. https://doi.org/10.32604/cmes.2019.07337.

Johnson, C. G., Kokelaar, B. P., Iverson, R. M., Logan, M., Lahusen, R. G., and Gray, J. M. N. T.: Grain-size segregation and levee formation in geophysical mass flows, J. Geophys. Res. Earth Surface, 117, 2012. https://doi.org/10.1029/2011JF002185

Kaitna, R., Palucis, M. C., Yohannes, B., Hill, K. M., and Dietrich, W. E.: Effects of coarse grain size distribution and fine particle content on pore fluid pressure and shear behavior in experimental debris flows, J. Geophys. Res. Earth Surf., 121, 415–441,2016. doi:10.1002/2015JF003725.

Likos, W. J., and Lu, N.: Water vapor sorption behavior of smectite-kaolinite mixtures. Clays Clay Mineral, 50, 553–561, 2002. https://doi.org/10.1346/000986002320679297/METRICS

McArdell, B. W., Bartelt, P., and Kowalski, J.: Field observations of basal forces and fluid pore pressure in a debris flow, Geophys. Res. Lett., 34, 2007. https://doi.org/10.1029/2006GL029183

McArdell, B. W., and Sartori, M.: The Illgraben torrent system. In E. Reynard (Ed.), World geomorphological landscapes, Landscapes and landforms of Switzerland (pp. 367-378), 2021. https://doi.org/10.1007/978-3-030-43203-4_25.

McArdell, B. W.: Field measurements of forces in debris flows at the Illgraben: implications for channel-bed erosion. Int. J. Erosion Control Eng., 9, 194-198, 2016. https://doi.org/10.13101/ijece.9.194

McArdell, B. W., Hirschberg, J., Graf, C., Boss, S., and Badoux, A.: Illgraben debris-flow characteristics 2019-2022. EnviDat. 2023. https://www.doi.org/10.16904/envidat.378.

Medina, V., Hürlimann, M. and Bateman, A.: Application of FLATModel, a 2D finite volume code, to debris flows in the northeastern part of the Iberian Peninsula. Landslides 5, 127–142, 2008. https://doi.org/10.1007/s10346-007-0102-3

Mikoš, M., and Bezak, N.: Debris flow modelling using RAMMS model in the Alpine environment with focus on the model parameters and main characteristics. Front. Earth Sci., 8 – 2020, 2021. https//doi.org/10.3389/feart.2020.605061.

Naef, D., Rickenmann, D., Rutschmann, P., and McArdell, B. W.: Comparison of flow resistance relations for debris flows using a one-dimensional finite element simulation model, Nat. Hazards Earth Sys. Sci., 6, 155–165, 2006. www.nat-hazards-earth-syst-sci.net/6/155/2006/

Formatted: Indent: Left: 0.85 cm, Hanging: 1 cm

Formatted: Indent: Left: 0.85 cm, Hanging: 1 cm

Formatted: Normal, Indent: Left: 0.85 cm, Hanging: 1 cm, Don't adjust space between Latin and Asian text, Don't adjust space between Asian text and numbers

Deleted: https://doi.org/10.1007/978-3-030-43203-4_25…

Formatted: Indent: Left: 0.85 cm, Hanging: 1 cm

Pierson, T. C.: Flow behavior of channelized debris flows, Mount St. Helens, Washington. In A. Abrahams (Ed.), Hillslope Processes (pp. 269–296), 1986.

Rickenmann, D.: Empirical Relationships for Debris Flows, Nat. Hazards, 19, 47–77, 1999.

Rietveld, H. M.: A profile refinement method for nuclear and magnetic structures, J. Applied Crystallography 2, 65–71, 1969. https://doi.org/10.1107/S0021889869006558

Salm, B.: Flow, flow transition and runout distances of flowing avalanches, Annal. Glaciol. 18, 221–226, 1993. https://doi.org/10.3189/S0260305500011551

Salm, B., Burkard, A., and Gubler, H. U.: Berechnung von Fliesslawinen. Eine Anleitung fuer Praktiker mit Beispielen, In Mitteilungen des Eidg. Institutes für Schnee- und Lawinenforschung (Vol. 47), 1990.

Scheiber, T., Pfiffner, O.A., and Schreurs, G.: Upper crustal deformation in continent-continent collision: A case study from the Bernhard nappe complex (Valais, Switzerland). Tectonics, 32, 1320-1342, 2013. https://doi.org/10.1002/tect.20080.

Schlunegger, F., Badoux, A., McArdell, B. W., Gwerder, C., Schnydrig, D., Rieke-Zapp, D., and Molnar, P.: Limits of sediment transfer in an alpine debris-flow catchment, Illgraben, Switzerland, Quat. Sci. Rev., 28, 1097–1105, 2009. https://doi.org/10.1016/j.quascirev.2008.10.025

Schlunegger, F., Garefalakis, P.: Einführung in die Sedimentologie. Schweizerbart, Stuttgart, 305 p., 2023.

Schürch, P., Densmore, A. L., Rosser, N. J., and McArdell, B. W.: Dynamic controls on erosion and deposition on debris-flow fans, Geology, 39, 827–830, 2011. https://doi.org/10.1130/G32103.1

Simoni, A., Mammoliti, M., and Graf, C.: Performance Of 2D debris flow simulation model RAMMS. Ann. Int. conf. GEOS, 2012. https://doi.org/10.5176/2251-3361_GEOS12.59

Swisstopo: Bundesamt für Landestopografie, 2022. https://www.swisstopo.admin.ch/de/geodata.html

Uchida, T., Nishiguchi, Y., McArdell, B. W., and Satofuka, Y.: The role of the phase shift of fine particles on debris flow behavior: a numerical simulation for a debris flow in Illgraben, Switzerland, Can. Geotech. J., 58, 23-34, 2021. https://doi.org/10.1139/cgj-2019-0452

Voellmy, A.: Über die Zerstörungskraft von Lawinen, Schweiz. Bauzeitschrift, 73, 212–217, 1995. https://doi.org/10.5169/seals-61891

WSL. RAMMS::DEBRISFLOW User Manual v1.8.0 (v1.8.0). WSL, 2022. https://ramms.slf.ch/en/modules/debrisflow.html

Deleted: .:;

Formatted: Indent: Left: 0.85 cm, Hanging: 1 cm

Formatted: German (Switzerland)

Deleted: https://doi.org/10.1016/j.quascirev.2008.10.025

Formatted: German (Switzerland)

Field Code Changed

Formatted: German (Switzerland)

Formatted: Indent: Left: 0.85 cm, Hanging: 1 cm

Deleted: Scotto Di Santolo

Deleted: Pellegrino, A.

Deleted: Evangelista, A.: Experimental study on the rheological behaviour of

Deleted: , Nat. Hazards Earth Sys. Sci., 10, 2507–2514, 2010.

Deleted: 5194/NHESS-10-2507-2010

Deleted:

Formatted: Normal, Indent: Left: 0.85 cm, Hanging: 1 cm, Don't adjust space between Latin and Asian text, Don't adjust space between Asian text and numbers

Deleted: an

Deleted:

Formatted: Indent: Left: 0.85 cm, Hanging: 1 cm

Page 4: [1] Deleted **Schlunegger, Fritz (GEO)** **28/12/2023 09:25:00**

Page 5: [2] Deleted **Schlunegger, Fritz (GEO)** **28/12/2023 09:25:00**

Appendix A: Measurements from monitoring station at the Illgraben

Event start	Front velocity CD 28-29 (m/s)	Max flow depth laser (m)	Max flow depth radar (m)	Mean bulk density laser (kg/m^3)	Peak velocity (quantile 0.99) laser CD 28-29 (m/s)	Peak velocity (quantile 0.99) radar CD 28-29 (m/s)	Peak discharge (quantile 0.99) laser CD 28-29 (m/s)	Volume laser CD 28-29 (m^3)	Flow duration (min)
21.06.2019 21:44	6.62	3.13	2.69	1870	6.55	6.57	147.61	97394	43
02.07.2019 01:26	3.86	1.75	1.73	1971	5.78	5.38	65.58	73188	52
26.07.2019 19:46	8.69	1.39	1.41	2223	9.74	9.98	93.26	113310	65
11.08.2019 19:07	6.95	1.81	1.89	2323	6.90	6.91	95.63	88064	88
20.08.2019 19:03	0.89	1.13	1.10	2031	1.36	1.36	8.06	6137	37
24.06.2021 17:11	8.18	2.40	2.49	1750	8.16	8.10	162.20	105032	38
06.07.2021 20:43	8.69	2.50	2.58	1605	8.65	8.67	186.61	76906	28
16.07.2021 05:43	2.78	2.38	2.44	1916	3.22	3.30	60.70	80879	77
07.08.2021 16:22	2.32	2.49	2.17	1884	2.89	2.74	41.19	38737	46
19.09.2021 08:57	1.25	1.13	1.22	1697	1.41	1.39	10.67	8538	43
05.06.2022 12:33	3.39	2.08	2.15	1690	4.14	4.32	55.42	39498	55
04.07.2022 22:54	8.18	2.49	2.60	1189	8.46	7.36	169.14	175929	39
08.09.2022 02:06	1.91	1.93	1.77	1592	1.85	1.87	20.94	9283	20

Appendix B: Video recordings of debris flows. The video camera is placed at the Survey Station (see Figure 1c in main text)

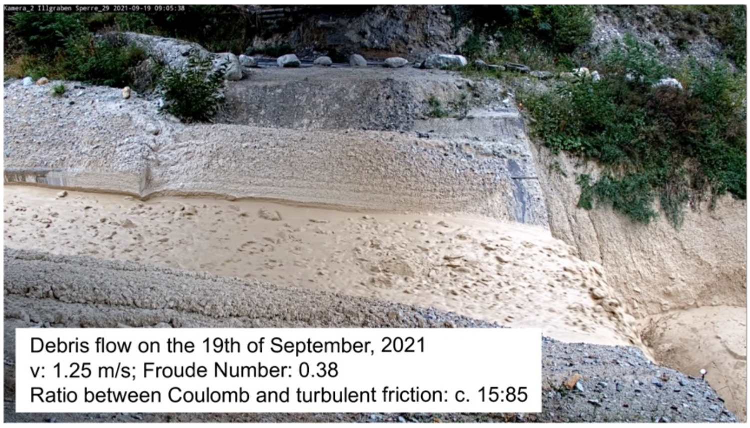

Debris flow on the 19th of September, 2021
v: 1.25 m/s; Froude Number: 0.38
Ratio between Coulomb and turbulent friction: c. 15:85

Debris flow on the 7th of August, 2021
v: 2.32 m/s; Froude Number: 0.47
Ratio between Coulomb and turbulent friction: c. 65:35

Debris flow on the 5th of June, 2022
v: 3.39 m/s; Froude Number: 0.75;
Ratio between Coulomb and turbulent friction: c. 90:10

Debris flow on the 24th of June, 2021
v: 8.18 m/s; Froude Number: 1.69
Ratio between Coulomb and turbulent friction: c. 45:55

Appendix C: Exemplary evaluation of the simulations of the debris flow event on 24.06.2021

Input data composed of raster and shape files, simulation settings and measurements from the monitoring station.

Event	**24.06.2021**
DTM	DTM_0.5.tif
DTM resolution [m]	0.5
calculation domain	calcdom.shp
release area	hydrograph.shp
stop parameter [%]	5
sim resolution [m]	0.5
end time [s]	600
dump step [s]	2
erosion layer	erosion.shp
erosion density [kg/m3]	2000
erosion rate [m/s]	0.025
pot. Erosion depth [per kPa]	0.1
critical shear stress [kPa]	1
max erosion depth [m]	1
density [kg/m3]	1750
inflow direction [°]	60
vol [m3]	105032
Qmax [m3/s]	162.2
t1 [s]	10
v [m/s]	8.18
Front velocity CD 28-29 (m/s)	8.18
Max flow depth laser (m)	2.4
Max flow depth radar (m)	2.49
Peak velocity (quantile 0.99) laser CD 28-29 (m/s)	8.16
Peak velocity (quantile 0.99) radar CD 28-29 (m/s)	8.1
Flow duration (min)	38
CD28-CD29	134m
CD27-CD29	460m
Froude number	1.69

Output data with velocity (v) and flow depth (av_maxd_P). These variables were compared with the results of the field survey to determine the best-fit simulation (green) for each *μ.* The z-values are calculated from the laser measurement (Max flow depth laser, see above).

Simulation	Mu []	Xi [m/s2]	v [m/s]	maxd_P1 [m]	maxd_P2 [m]	maxd_P3 [m]	maxd_P4 [m]	av_maxd_P [m]	Froude number []	Qmax [m3/s]	z value laser	z value radar
1	0.02	1400	8.9	1.99	2.30	2.54	2.93	2.44	1.82	140	0.09	0.09
2	0.02	800	7.9	3.00	2.94	2.84	3.03	2.95	1.47	130	0.23	0.19
3	0.02	1000	7.9	2.63	2.71	2.62	2.89	2.71	1.53	147	0.13	0.10
4	0.02	1200	8.4	2.22	2.38	2.40	2.71	2.43	1.72	140	0.03	0.04
5	0.04	1500	7.9	2.94	2.86	2.65	2.86	2.83	1.50	128	0.18	0.14
6	0.04	2000	8.4	2.60	2.64	2.57	2.69	2.63	1.66	140	0.10	0.06
7	0.04	2500	8.4	2.45	2.55	2.54	2.78	2.58	1.67	137	0.08	0.05
8	0.04	3000	8.4	2.04	2.55	2.69	2.97	2.56	1.68	142	0.07	0.04
9	0.06	12000	7.9	3.21	3.12	3.00	3.12	3.11	1.43	138	0.30	0.25
10	0.06	8000	7.9	3.31	3.22	3.20	3.50	3.31	1.39	124	0.38	0.33
11	0.06	9000	8.4	3.38	3.26	3.16	3.39	3.30	1.48	128	0.37	0.33
12	0.06	10000	7.9	3.19	3.09	2.97	3.22	3.12	1.43	135	0.30	0.25
13	0.06	14000	8.4	2.62	2.59	2.67	2.95	2.71	1.63	135	0.13	0.09
14	0.01	800	8.4	2.62	2.69	2.56	2.87	2.69	1.64	138	0.12	0.08
15	0.01	1000	8.4	2.18	2.33	2.49	2.84	2.46	1.71	138	0.04	0.03
16	0.01	1200	8.9	1.90	2.35	2.68	3.26	2.55	1.78	142	0.11	0.09
17	0.03	1000	7.9	2.94	2.87	2.70	3.04	2.89	1.48	139	0.21	0.16
18	0.03	1500	8.4	2.46	2.59	2.49	2.78	2.58	1.67	144	0.08	0.05
19	0.03	2000	8.9	2.07	2.53	2.71	2.97	2.57	1.77	145	0.11	0.09
20	0.03	2500	9.6	1.95	2.31	2.65	3.05	2.49	1.94	136	0.18	0.17
21	0.04	3500	8.9	1.71	2.12	2.66	3.04	2.38	1.84	136	0.09	0.10
22	0.05	8000	8.9	1.70	2.13	2.51	2.91	2.31	1.87	137	0.10	0.11
23	0.05	10000	8.9	2.04	2.48	2.77	3.10	2.60	1.76	137	0.12	0.10
24	0.05	12000	8.9	1.77	2.45	2.94	3.35	2.63	1.75	136	0.13	0.10
25	0.05	14000	8.9	1.82	2.06	2.55	3.27	2.43	1.82	136	0.09	0.09
26	0.05	6000	8.4	2.16	2.54	2.59	2.80	2.52	1.69	146	0.06	0.03
27	0.06	16000	8.4	2.87	2.73	2.70	2.94	2.81	1.60	133	0.17	0.13
28	0.04	4000	8.9	1.99	2.48	2.70	3.12	2.57	1.77	139	0.11	0.09
29	0.02	1600	7.6	2.09	2.47	2.65	3.13	2.59	1.51	139	0.10	0.08
30	0.02	4000	11.2	1.99	1.93	2.19	2.42	2.13	2.45	152	0.39	0.40
31	0.04	3200	8.9	1.80	2.29	2.65	3.00	2.44	1.82	135	0.09	0.09
32	0.05	7000	8.4	1.77	2.42	2.67	2.93	2.45	1.71	139	0.03	0.03
33	0.06	15000	7.9	2.62	2.58	2.71	3.05	2.74	1.52	137	0.15	0.11

Appendix D: Details on the modelling approach

Information on the number of model runs, the intervals between the μ– and ξ–values upon modelling, and event-specific and general input values that were used opon modelling. Appendix B also lists the results of the model runs per event where the model results and observations had a best fit.

Number of model runs

Event	# of simulations	best z-value
21.06.19	43	0.06
02.07.19	34	0.32
11.08.19	41	0.13
20.08.19	36	0.02
24.06.21	37	0.03
06.07.21	38	0.03
16.07.21	30	0.03
07.08.21	23	0.23
19.09.21	33	0.11
05.06.22	12	0.01
04.07.22	13	0.02
08.09.22	20	0.34
Total	360	

Variations of μ and ξ values

μ	0.01
ξ	1 to > 1000

For μ we only used the values 0.01, 0.02, 0.03, 0.04, 0.05 and 0.06 upon modelling.
Also upon modeling, the intervals between the ξ–values were 1 for those models where we set μ =1. For larger μ–values, we increased the intervals between the subsequent ξ–values to >> 1000. We iteratively changed the values until we found a best-fit between model results and observations.

Input for RAMMS, which were not event-specific

DTM	DTM_0.5.tif
DTM resolution [m]	0.5
calculation domain	calcdom.shp
release area	hydrograph.shp
stop parameter [%]	5
sim resolution [m]	0.5
end time [s]	1000
dump step [s]	2
erosion layer	erosion.shp
erosion density [kg/m3]	2000
erosion rate [m/s]	0.025
pot. Erosion depth [per kPa]	0.1
critical shear stress [kPa]	1
max erosion depth [m]	1
inflow direction [°]	60
t1 Hydrograph [s]	10

Input for RAMMS, which were event-specific

Event	21.06.19	02.07.19	11.08.19	20.08.19	24.06.21	06.07.21	16.07.21	07.08.21	19.09.21	05.06.22	04.07.22	08.09.22
density [kg/m^3]	1870	1971	2323	2031	1750	1605	1916	1884	1697	1690	1189	1592
vol [m^3]	97394	73188	88064	6137	105032	76906	80879	38737	8538	39498	175929	9283
Qmax [m^3/s]	147.61	65.58	95.63	8.06	162.2	186.61	60.7	41.19	10.67	55.42	169.14	20.94
Front velocity CD 28-29 [m/s]	6.62	3.86	6.95	0.89	8.18	8.69	2.78	2.32	1.25	3.39	8.18	1.91
Max flow depth laser [m]	3.13	1.75	1.81	1.13	2.4	2.5	2.38	2.49	1.13	2.08	2.49	1.93
Max flow depth radar [m]	2.69	1.73	1.89	1.1	2.49	2.58	2.44	2.17	1.22	2.15	2.6	1.77
Froude Number	1.19	0.93	1.65	0.27	1.69	1.75	0.58	0.47	0.38	0.75	1.66	0.44

Best-fit outputs of RAMMs models

Event	21.06.19	02.07.19	11.08.19	20.08.19	24.06.21	06.07.21	16.07.21	07.08.21	19.09.21	05.06.22	04.07.22	08.09.22
Front velocity CD 28-29 [m/s]	6.7	3.9	7.4	0.9	8.4	8.9	2.8	2.31	1.24	3.35	8.38	1.76
Max flow depth [m]	2.96	2.32	2.02	1.15	2.43	2.47	2.32	1.91	1.01	2.09	2.5	1.29
Froude number	1.24	0.83	1.66	0.27	1.72	1.81	0.59	0.53	0.39	0.74	1.69	0.49
Qmax [m^3/s]	122	54	78	7	140	158	48	35	9	40	143	17
μ	0.06	0.06	0.06	0.01	0.02	0.05	0.05	0.04	0.01	0.06	0.01	0.01
ξ	4500	1000	8500	12	1200	10000	170	105	25	700	1000	50
z-value	0.06	0.32	0.13	0.02	0.03	0.03	0.03	0.23	0.11	0.01	0.02	0.34

Appendix E: Measured and calculated properties for each flow (v, flow depth, Froude number, volume, density), best-fit model results (μ, ξ, z) and related total (S) and Coulomb and turbulent frictions

For each debris flow event, distinct μ- ξ pairs can be used to successfully model the flow properties such as flow velocity and flow depth. The best-fit solutions between model results and observations, characterized by the lowest z-values, are highlighted by the yellow bar. The values of these best-fit results are displayed in Table E.

Event	v [m/s]	Flow Depth [m]	Froude Number	Volume (m^3)	Density (kg/m^3)	μ	ξ	z	Total Friction S [Pa]	Coulomb Friction [Pa]	Turbulent Friction [Pa]	Coulomb Friction [%]	Turbulent Friction [%]
21.06.19	6.6	3.1	1.19	97394	1870	0.01	500	0.07	2166	568	1598	26	74
21.06.19	6.6	3.1	1.19	97394	1870	0.02	550	0.10	2588	1135	1453	44	56
21.06.19	6.6	3.1	1.19	97394	1870	0.03	800	0.10	2702	1703	999	63	37
21.06.19	6.6	3.1	1.19	97394	1870	0.04	1000	0.11	3069	2270	799	74	26
21.06.19	6.6	3.1	1.19	97394	1870	0.05	1300	0.11	3452	2838	615	82	18
21.06.19	6.6	3.1	1.19	97394	1870	0.06	4500	0.06	3583	3405	178	95	5
02.07.19	3.9	1.8	0.93	73188	1971	0.01	200	0.37	1818	347	1470	19	81
02.07.19	3.9	1.8	0.93	73188	1971	0.02	250	0.37	1871	695	1176	37	63
02.07.19	3.9	1.8	0.93	73188	1971	0.03	300	0.37	2022	1042	980	52	48
02.07.19	3.9	1.8	0.93	73188	1971	0.04	350	0.36	2230	1389	840	62	38
02.07.19	3.9	1.8	0.93	73188	1971	0.05	600	0.35	2227	1737	490	78	22
02.07.19	3.9	1.8	0.93	73188	1971	0.06	1000	0.32	2378	2084	294	88	12
11.08.19	7	1.8	1.65	88064	2323	0.01	1000	0.16	1526	409	1117	27	73
11.08.19	7	1.8	1.65	88064	2323	0.02	1000	0.18	1935	819	1117	42	58
11.08.19	7	1.8	1.65	88064	2323	0.03	2500	0.21	1675	1228	447	73	27
11.08.19	7	1.8	1.65	88064	2323	0.04	2000	0.18	2196	1637	558	75	25
11.08.19	7	1.8	1.65	88064	2323	0.05	8000	0.14	2186	2047	140	94	6
11.08.19	7	1.8	1.65	88064	2323	0.06	8500	0.13	2588	2456	131	95	5
20.08.19	0.9	1.1	0.27	6137	2031	0.01	12	0.02	1564	219	1345	14	86
20.08.19	0.9	1.1	0.27	6137	2031	0.02	13	0.03	1679	437	1241	26	74
20.08.19	0.9	1.1	0.27	6137	2031	0.03	12	0.10	2001	656	1345	33	67
20.08.19	0.9	1.1	0.27	6137	2031	0.04	21	0.12	1643	875	769	53	47
20.08.19	0.9	1.1	0.27	6137	2031	0.05	20	0.17	1901	1094	807	58	42
20.08.19	0.9	1.1	0.27	6137	2031	0.06	30	0.25	1850	1312	538	71	29
24.06.21	8.2	2.4	1.69	105032	1750	0.01	1000	0.04	1566	411	1154	26	74
24.06.21	8.2	2.4	1.69	105032	1750	0.02	1200	0.03	1784	822	962	46	54
24.06.21	8.2	2.4	1.69	105032	1750	0.03	1500	0.08	2003	1234	770	62	38
24.06.21	8.2	2.4	1.69	105032	1750	0.04	3000	0.07	2030	1645	385	81	19
24.06.21	8.2	2.4	1.69	105032	1750	0.05	7000	0.03	2221	2056	165	93	7
24.06.21	8.2	2.4	1.69	105032	1750	0.06	14000	0.13	2550	2467	82	97	3
06.07.21	8.7	2.5	1.75	76906	1605	0.01	800	0.06	1883	393	1490	21	79
06.07.21	8.7	2.5	1.75	76906	1605	0.02	1500	0.06	1580	786	794	50	50
06.07.21	8.7	2.5	1.75	76906	1605	0.03	1750	0.08	1860	1179	681	63	37
06.07.21	8.7	2.5	1.75	76906	1605	0.04	3000	0.09	1969	1571	397	80	20
06.07.21	8.7	2.5	1.75	76906	1605	0.05	10000	0.03	2083	1964	119	94	6
06.07.21	8.7	2.5	1.75	76906	1605	0.06	25000	0.12	2405	2357	48	98	2
16.07.21	2.8	2.4	0.58	80879	1916	0.01	65	0.04	2717	450	2267	17	83
16.07.21	2.8	2.4	0.58	80879	1916	0.02	75	0.04	2865	900	1965	31	69
16.07.21	2.8	2.4	0.58	80879	1916	0.03	95	0.05	2902	1351	1551	47	53
16.07.21	2.8	2.4	0.58	80879	1916	0.04	125	0.07	2980	1801	1179	60	40
16.07.21	2.8	2.4	0.58	80879	1916	0.05	170	0.03	3118	2251	867	72	28
16.07.21	2.8	2.4	0.58	80879	1916	0.06	280	0.04	3227	2701	526	84	16

07.08.21	2.3	2.5	0.47	38737	1884	0.01	50	0.25	2417	461	1955	19	81
07.08.21	2.3	2.5	0.47	38737	1884	0.02	65	0.26	2426	922	1504	38	62
07.08.21	2.3	2.5	0.47	38737	1884	0.03	65	0.25	2888	1383	1504	48	52
07.08.21	2.3	2.5	0.47	38737	1884	0.04	105	0.23	2776	1845	931	66	34
07.08.21	2.3	2.5	0.47	38737	1884	0.05	150	0.25	2957	2306	652	78	22
07.08.21	2.3	2.5	0.47	38737	1884	0.06	230	0.27	3192	2767	425	87	13
19.09.21	1.3	1.1	0.38	8538	1697	0.01	25	0.11	1308	183	1125	14	86
19.09.21	1.3	1.1	0.38	8538	1697	0.02	30	0.12	1303	366	938	28	72
19.09.21	1.3	1.1	0.38	8538	1697	0.03	43	0.17	1203	548	654	46	54
19.09.21	1.3	1.1	0.38	8538	1697	0.04	50	0.18	1294	731	563	57	43
19.09.21	1.3	1.1	0.38	8538	1697	0.05	80	0.23	1265	914	352	72	28
19.09.21	1.3	1.1	0.38	8538	1697	0.06	160	0.20	1272	1097	176	86	14
05.06.22	3.4	2.1	0.75	39498	1690	0.01	130	0.06	1822	347	1474	19	81
05.06.22	3.4	2.1	0.75	39498	1690	0.02	160	0.05	1893	695	1198	37	63
05.06.22	3.4	2.1	0.75	39498	1690	0.03	210	0.05	1955	1042	913	53	47
05.06.22	3.4	2.1	0.75	39498	1690	0.04	260	0.04	2127	1390	737	65	35
05.06.22	3.4	2.1	0.75	39498	1690	0.05	400	0.03	2216	1737	479	78	22
05.06.22	3.4	2.1	0.75	39498	1690	0.06	700	0.01	2359	2085	274	88	12
04.07.22	8.2	2.5	1.66	175929	1189	0.01	1000	0.02	1075	291	784	27	73
04.07.22	8.2	2.5	1.66	175929	1189	0.02	1200	0.04	1236	582	654	47	53
04.07.22	8.2	2.5	1.66	175929	1189	0.03	1500	0.07	1396	873	523	63	37
04.07.22	8.2	2.5	1.66	175929	1189	0.04	2000	0.09	1556	1164	392	75	25
04.07.22	8.2	2.5	1.66	175929	1189	0.05	6000	0.04	1586	1455	131	92	8
04.07.22	8.2	2.5	1.66	175929	1189	0.06	20000	0.08	1785	1746	39	98	2
08.09.22	1.9	1.9	0.44	9283	1592	0.01	50	0.34	1424	296	1128	21	79
08.09.22	1.9	1.9	0.44	9283	1592	0.02	60	0.36	1532	592	940	39	61
08.09.22	1.9	1.9	0.44	9283	1592	0.03	80	0.37	1593	888	705	56	44
08.09.22	1.9	1.9	0.44	9283	1592	0.04	125	0.39	1636	1185	451	72	28
08.09.22	1.9	1.9	0.44	9283	1592	0.05	150	0.35	1857	1481	376	80	20
08.09.22	1.9	1.9	0.44	9283	1592	0.06	350	0.41	1938	1777	161	92	8

Appendix F: Best-fit model results per event

Each debris flow event can be characterized by a distinct μ- ξ pair with a lowest z-value. See Table in Appendix B for best-fit μ- ξ pairs per event.

Event	v [m/s]	Flow Depth [m]	Froude Number	Volume (m^3)	Density (kg/m^3)	μ	ξ	z	Total Friction [Pa]	Coulomb Friction [Pa]	Turbulent Friction [Pa]	Coulomb Friction [%]	Turbulent Friction [%]
21.06.19	6.6	3.1	1.19	97394	1870	0.06	4500	0.06	3583	3405	178	95	5
02.07.19	3.9	1.8	0.93	73188	1971	0.06	1000	0.32	2378	2084	294	88	12
11.08.19	7	1.8	1.65	88064	2323	0.06	8500	0.13	2588	2456	131	95	5
20.08.19	0.9	1.1	0.27	6137	2031	0.01	12	0.02	1564	219	1345	14	86
24.06.21	8.2	2.4	1.69	105032	1750	0.02	1200	0.03	1784	822	962	46	54
06.07.21	8.7	2.5	1.75	76906	1605	0.05	10000	0.03	2083	1964	119	94	6
16.07.21	2.8	2.4	0.58	80879	1916	0.05	170	0.03	3118	2251	867	72	28
07.08.21	2.3	2.5	0.47	38737	1884	0.04	105	0.23	2776	1845	931	66	34
19.09.21	1.3	1.1	0.38	8538	1697	0.01	25	0.11	1308	183	1125	14	86
05.06.22	3.4	2.1	0.75	39498	1690	0.06	700	0.01	2359	2085	274	88	12
04.07.22	8.2	2.5	1.66	175929	1189	0.01	1000	0.02	1075	291	784	27	73
08.09.22	1.9	1.9	0.44	9283	1592	0.01	50	0.34	1424	296	1128	21	79

Appendix G: Grain size data

Weight percent passing per mesh size for each sample and complete overview of results from sieving.

Mesh size [mm]	21.06.2019	02.07.2019	26.07.2019	11.08.2019	20.08.2019	24.06.2021	06.07.2021	16.07.2021	07.08.2021	19.09.2021	04.10.2021	05.06.2022	04.07.2022	08.09.2022
16.0000	100.0	100.0	100.0	100.0	100.0	100.0	100.0	100.0	100.0	100.0	100.0	100.0	100.0	100.0
8.0000	85.0	99.8	88.3	86.5	87.2	91.8	86.2	80.6	85.3	89.0	88.1	86.4	81.7	84.4
4.0000	73.7	97.5	78.6	76.3	76.5	83.6	75.1	69.5	74.8	79.9	79.7	78.2	70.5	74.5
2.0000	66.0	92.5	71.0	68.5	69.0	76.7	68.0	63.1	68.6	73.5	73.7	71.5	63.2	68.1
1.0000	59.0	85.6	63.8	61.1	62.1	69.9	61.1	58.6	63.2	67.7	68.5	64.5	56.8	61.8
0.5000	52.0	77.6	56.7	53.8	55.3	62.5	53.7	54.4	57.6	60.9	62.6	56.6	50.2	54.9
0.2500	44.8	68.6	48.6	50.1	47.8	53.7	46.7	49.0	50.7	52.4	56.1	48.8	43.2	47.5
0.1250	37.6	59.0	41.3	44.0	40.6	44.9	39.1	42.1	43.4	43.6	47.8	41.5	35.8	40.4
0.0630	31.7	49.1	34.4	36.3	34.1	37.0	32.0	35.4	35.9	35.7	39.8	34.0	29.4	33.0
0.0462	28.3	44.4	30.5	32.6	30.7	33.2	28.7	32.2	32.3	32.1	36.0	29.8	26.3	29.3
0.0339	24.8	39.6	26.1	28.3	27.0	28.9	24.5	28.0	27.7	27.0	30.5	25.7	22.8	25.8
0.0224	19.4	30.8	20.1	21.5	20.6	22.9	18.9	22.1	21.7	20.4	23.6	19.9	17.3	20.4
0.0135	13.0	21.3	13.3	14.0	14.4	15.2	13.0	15.1	14.4	13.4	15.8	13.2	12.0	13.0
0.0081	7.9	12.5	8.0	8.4	8.9	8.9	7.1	9.5	8.6	8.0	9.5	8.3	7.1	7.9
0.0050	5.1	7.8	5.3	5.4	5.7	5.7	4.5	5.8	5.0	5.0	5.9	5.4	4.8	5.3
0.0032	3.2	4.8	3.5	3.6	3.7	3.8	3.1	4.1	3.4	3.2	4.0	3.8	3.5	3.9
0.0015	1.3	2.5	1.8	1.6	2.1	2.4	1.9	2.2	1.5	1.8	2.8	2.3	1.9	2.3
0.0000	0.0	0.0	0.0	0.0	0.0	0.0	0.0	0.0	0.0	0.0	0.0	0.0	0.0	0.0

	Event	21.06.19			02.07.19			26.07.19			11.08.19			20.08.19		
	Sample mass [g]	1958.7			1772.4			2856.1			3299.7			3001.5		
Method	Mesh size [mm]	Weight [g]	Weight % passing	Weight % passing max. 16 mm	Weight [g]	Weight % passing	Weight % passing max. 16 mm	Weight [g]	Weight % passing	Weight % passing max. 16 mm	Weight [g]	Weight % passing	Weight % passing max. 16 mm	Weight [g]	Weight % passing	Weight % passing max. 16 mm
dry sieving	125.0000	0.0	100.0	100.0	0.0	100.0	100.0	0.0	100.0	100.0	0.0	100.0	100.0	0.0	100.0	100.0
	63.0000	0.0	100.0	100.0	0.0	100.0	100.0	0.0	100.0	100.0	0.0	100.0	100.0	0.0	100.0	100.0
	31.5000	0.0	100.0	100.0	0.0	100.0	100.0	55.7	98.1	100.0	0.0	100.0	100.0	0.0	100.0	100.0
	16.0000	365.0	81.4	100.0	0.0	100.0	100.0	158.9	92.5	100.0	472.6	85.7	100.0	327.9	89.1	100.0
	8.0000	239.7	69.1	85.0	3.4	99.8	99.8	308.3	81.7	88.3	380.6	74.1	86.5	341.7	77.7	87.2
	4.0000	180.2	59.9	73.7	40.5	97.5	97.5	258.1	72.7	78.6	288.3	65.4	76.3	287.4	68.1	76.5
	2.0000	122.5	53.7	66.0	88.3	92.5	92.5	199.3	65.7	71.0	220.4	58.7	68.5	198.8	61.5	69.0
	1.0000	110.5	48.0	59.0	123.6	85.6	85.6	189.9	59.0	63.8	211.7	52.3	61.1	184.7	55.3	62.1
	0.5000	111.4	42.3	52.0	142.0	77.6	77.6	187.3	52.5	56.7	206.6	46.1	53.8	182.5	49.3	55.3
wet sieving	0.2500		36.4	44.8		68.6	68.6		45.0	48.6		42.9	50.1		42.6	47.8
	0.1250		30.6	37.6		59.0	59.0		38.2	41.3		37.7	44.0		36.2	40.6
	0.0630		25.8	31.7		49.1	49.1		31.8	34.4		31.1	36.3		30.4	34.1
slurry test	0.0462		23.0	28.3		44.4	44.4		28.2	30.5		27.9	32.6		27.4	30.7
	0.0339		20.2	24.8		39.6	39.6		24.2	26.1		24.2	28.3		24.0	27.0
	0.0224		15.8	19.4		30.8	30.8		18.6	20.1		18.4	21.5		18.3	20.6
	0.0135		10.6	13.0		21.3	21.3		12.3	13.3		12.0	14.0		12.8	14.4
	0.0081		6.4	7.9		12.5	12.5		7.4	8.0		7.2	8.4		7.9	8.9
	0.0050		4.1	5.1		7.8	7.8		4.9	5.3		4.6	5.4		5.1	5.7
	0.0032		2.6	3.2		4.8	4.8		3.2	3.5		3.1	3.6		3.3	3.7
	0.0015		1.1	1.3		2.5	2.5		1.7	1.8		1.4	1.6		1.9	2.1
	0.0000		0.0	0.0		0.0	0.0		0.0	0.0		0.0	0.0		0.0	0.0

	Event	24.06.21			06.07.21			16.07.21			07.08.21			19.09.21		
	Sample mass [g]	2652.5			3341.9			2511.2			2965.8			2553.6		
Method	Mesh size [mm]	Weight [g]	Weight % passing	Weight % passing max. 16 mm	Weight [g]	Weight % passing	Weight % passing max. 16 mm	Weight [g]	Weight % passing	Weight % passing max. 16 mm	Weight [g]	Weight % passing	Weight % passing max. 16 mm	Weight [g]	Weight % passing	Weight % passing max. 16 mm
dry sieving	125.0000	0.0	100.0	100.0	0.0	100.0	100.0	0.0	100.0	100.0	0.0	100.0	100.0	0.0	100.0	100.0
	63.0000	0.0	100.0	100.0	0.0	100.0	100.0	0.0	100.0	100.0	0.0	100.0	100.0	0.0	100.0	100.0
	31.5000	0.0	100.0	100.0	296.0	83.3	100.0	434.0	84.8	100.0	602.3	81.7	100.0	212.2	92.9	100.0
	16.0000	102.7	94.8	100.0	290.2	66.9	100.0	615.7	63.2	100.0	795.1	57.7	100.0	405.6	79.4	100.0
	8.0000	152.8	87.0	91.8	163.4	57.7	86.2	349.9	51.0	80.6	279.6	49.2	85.3	261.1	70.7	89.0
	4.0000	151.6	79.2	83.6	131.8	50.3	75.1	200.7	44.0	69.5	199.4	43.1	74.8	217.9	63.5	79.9
	2.0000	127.9	72.7	76.7	84.7	45.5	68.0	116.3	39.9	63.1	119.0	39.5	68.6	151.8	58.4	73.5
	1.0000	125.9	66.3	69.9	81.8	40.9	61.1	80.2	37.1	58.6	102.7	36.4	63.2	139.3	53.8	67.7
	0.5000	138.8	59.2	62.5	87.4	35.9	53.7	76.7	34.4	54.4	106.6	33.2	57.6	162.5	48.3	60.9
wet sieving	0.2500		50.9	53.7		31.2	46.7		31.0	49.0		29.3	50.7		41.6	52.4
	0.1250		42.5	44.9		26.2	39.1		26.6	42.1		25.0	43.4		34.6	43.6
	0.0630		35.1	37.0		21.4	32.0		22.4	35.4		20.7	35.9		28.3	35.7
slurry test	0.0462		31.5	33.2		19.2	28.7		20.3	32.2		18.6	32.3		25.5	32.1
	0.0339		27.4	28.9		16.4	24.5		17.7	28.0		15.9	27.7		21.5	27.0
	0.0224		21.7	22.9		12.7	18.9		14.0	22.1		12.5	21.7		16.2	20.4
	0.0135		14.4	15.2		8.7	13.0		9.5	15.1		8.3	14.4		10.7	13.4
	0.0081		8.4	8.9		4.8	7.1		6.0	9.5		5.0	8.6		6.4	8.0
	0.0050		5.4	5.7		3.0	4.5		3.6	5.8		2.9	5.0		4.0	5.0
	0.0032		3.6	3.8		2.1	3.1		2.6	4.1		1.9	3.4		2.5	3.2
	0.0015		2.3	2.4		1.3	1.9		1.4	2.2		0.9	1.5		1.4	1.8
	0.0000		0.0	0.0		0.0	0.0		0.0	0.0		0.0	0.0		0.0	0.0

	Event	04.10.21			05.06.22			04.07.22			08.09.22		
	Sample mass [g]	2788.3			2866.9			2677.2			3400.6		
Method	Mesh size [mm]	Weight [g]	Weight % passing	Weight % passing max. 16 mm	Weight [g]	Weight % passing	Weight % passing max. 16 mm	Weight [g]	Weight % passing	Weight % passing max. 16 mm	Weight [g]	Weight % passing	Weight % passing max. 16 mm
dry sieving	125.0000	0.0	100.0	100.0	0.0	100.0	100.0	0.0	100.0	100.0	0.0	100.0	100.0
	63.0000	0.0	100.0	100.0	0.0	100.0	100.0	0.0	100.0	100.0	0.0	100.0	100.0
	31.5000	147.8	92.5	100.0	116.2	93.4	100.0	315.5	89.0	100.0	167.8	94.9	100.0
	16.0000	284.9	77.9	100.0	312.6	75.8	100.0	553.6	69.6	100.0	527.1	78.9	100.0
	8.0000	180.9	68.7	88.1	182.8	65.5	86.4	364.6	56.8	81.7	406.8	66.6	84.4
	4.0000	128.7	62.1	79.7	109.5	59.3	78.2	221.3	49.1	70.5	256.4	58.8	74.5
	2.0000	92.4	57.4	73.7	90.7	54.2	71.5	145.4	44.0	63.2	168.7	53.7	68.1
	1.0000	78.2	53.4	68.5	93.5	48.9	64.5	126.4	39.5	56.8	162.7	48.8	61.8
	0.5000	89.8	48.8	62.6	106.9	42.9	56.6	132.2	34.9	50.2	181.1	43.3	54.9
wet sieving	0.2500		43.7	56.1		37.0	48.8		30.1	43.2		37.5	47.5
	0.1250		37.2	47.8		31.5	41.5		24.9	35.8		31.9	40.4
	0.0630		31.0	39.8		25.8	34.0		20.4	29.4		26.1	33.0
slurry test	0.0462		28.0	36.0		22.6	29.8		18.3	26.3		23.1	29.3
	0.0339		23.8	30.5		19.5	25.7		15.9	22.8		20.4	25.8
	0.0224		18.4	23.6		15.1	19.9		12.1	17.3		16.1	20.4
	0.0135		12.3	15.8		10.0	13.2		8.4	12.0		10.3	13.0
	0.0081		7.4	9.5		6.3	8.3		4.9	7.1		6.2	7.9
	0.0050		4.6	5.9		4.1	5.4		3.4	4.8		4.2	5.3
	0.0032		3.1	4.0		2.9	3.8		2.5	3.5		3.0	3.9
	0.0015		2.2	2.8		1.8	2.3		1.3	1.9		1.8	2.3
	0.0000		0.0	0.0		0.0	0.0		0.0	0.0		0.0	0.0

Appendix H: Results of powder x-ray diffraction analysis

Measured weight percent per mineral for all four analyzed samples.

	02.07.2019	26.07.2019	20.08.2019	16.07.2021
Albite	2.0	2.0	1.8	2.0
Calcite	10.6	7.4	10.2	17.9
Dolomite	24.4	16.7	23.7	19.4
Muscovite	17.7	22.2	19.6	18.2
Orthoclase	3.4	2.9	2.8	3.0
Quartz	29.9	36.0	29.2	30.9
Chlorite	0.3	0.1	0.2	0.0
Illite	11.3	12.1	11.7	8.4
Kaolinite	0.0	0.1	0.1	0.0
Smektite	0.2	0.6	0.7	0.3